Volume 72, Number 6
March 15, 2008

ELSEVIER

Geochimica et Cosmochimica Acta

JOURNAL OF THE GEOCHEMICAL SOCIETY
AND THE METEORITICAL SOCIETY

Available online at www.sciencedirect.com
ScienceDirect
Geochimica et Cosmochimica Acta 72 (2008) 1638–1659
Geochimica et Cosmochimica Acta
www.elsevier.com/locate/gca

The partitioning behavior of silver in a vapor–brine–rhyolite melt assemblage

Adam C. Simon [a,*], Thomas Pettke [b], Philip A. Candela [c], Philip M. Piccoli [c]

[a] Department of Geoscience, University of Nevada, Las Vegas, NV 89154-4010, USA
[b] Institute of Geological Sciences, University of Bern, Baltzerstrasse 1+3, CH-3012 Bern, Switzerland
[c] Laboratory for Mineral Deposits Research, Department of Geology, University of Maryland, College Park, MD 20742, USA

Received 12 June 2007; accepted in revised form 9 January 2008; available online 26 January 2008

Abstract

The partitioning of silver in a sulfur-free rhyolite melt–vapor–brine assemblage has been quantified at 800 °C, pressures of 100 and 140 MPa and $f_{O_2} \approx$ NNO (nickel–nickel oxide). Silver solubility ($\pm 2\sigma$) in rhyolite increases 5-fold from 105 ± 21 to 675 ± 98 μg/g as pressure increases from 100 to 140 MPa. Nernst-type partition coefficients ($D^{i,j}_{Ag} \pm 2\sigma$) describing the mass transfer of silver at 100 MPa between vapor and melt, brine and melt and vapor and brine are 32 ± 30, 1151 ± 238 and 0.026 ± 0.004, respectively. At 140 MPa, values for $D^{i,j}_{Ag}(\pm 2\sigma)$ for vapor and melt, brine and melt, and vapor and brine are 32 ± 10, 413 ± 172 and 0.06 ± 0.03, respectively. Apparent equilibrium constant values ($\pm 2\sigma$) describing the exchange of silver and sodium between vapor and melt, $K^{v/m}_{Ag,Na}$, at 100 and 140 MPa are 105 ± 68 and 14 ± 6. The average values ($\pm 2\sigma$) for silver and sodium exchange between brine and melt, $K^{b/m}_{Ag,Na}$, at 100 and 140 MPa are 313 ± 288 and 65 ± 12. These data indicate that the mass transfer of silver from rhyolite melt to an exsolved volatile phase(s) is enhanced at 100 MPa relative to 140 MPa, suggesting that decompression increases the silver ore-generative potential of an evolving silicate magma. Model calculations using the new data suggest that the evolution of low-density, aqueous fluid (i.e., vapor) may be responsible for the the silver tonnage of many porphyry-type and perhaps epithermal-type ore deposits. For example, Halter et al. (Halter W. E., Pettke T. and Heinrich C. A. (2002) The origin of Cu/Au ratios in porphyry-type ore deposits. *Science* **296**, 1842–1844) used detailed silicate and sulfide melt inclusion and vapor and brine fluid inclusions analyses to estimate a melt volume on the order of 15 km^3 to satisfy the copper budget at the Bajo de la Alumbrera copper-, gold-, silver-ore deposit. Using their melt volume estimate with the data presented here, model calculations for a 15-km^3 felsic melt, saturated with pyrrhotite and magnetite, suggest that a low-salinity magmatic vapor may scavenge on the order of 7×10^{12} g of silver from the melt. This quantity of silver exceeds the discovered 2×10^9 g of Ag at Alumbrera. Calculated tonnages for numerous other deposits yield similar results. The excess silver in the vapor, remaining after porphyry formation, is then available to precipitate at lower *PT*conditions in the stratigraphically higher epithermal environment. These data suggest that silver, and perhaps other ore metals, in the porphyry-epithermal continuum may be derived solely from the time-integrated flux of dominantly low-salinity vapor exsolved from a series of sequential magma batches.

1. INTRODUCTION

Porphyry- and epithermal-type ore deposits together contain on the order 10^{11} tons of Ag (Singer, 1995). Fluid inclusion homogenization temperatures and alteration mineralogy (Simmons et al., 2005; Seedorff et al., 2005) have been used to constrain the pressure–temperature (*PT*) conditions at which Ag deposition occurs in the porphyry (50–100 MPa and 300–500 °C) to epithermal (10–50 MPa and 100–300 °C) continuum. To build predictive models for Ag deposition from circulating magmatic–hydrothermal aqueous fluids, there have been numerous experimental

* Corresponding author. Fax: +1 702 895 4064.
E-mail address: adam.simon@unlv.edu (A.C. Simon).

0016-7037/$ - see front matter © 2008 Elsevier Ltd. All rights reserved.
doi:10.1016/j.gca.2008.01.003

studies performed with the unifying goal of quantifying the behavior of Ag in aqueous fluids at these *PT* conditions (Seward, 1976; Kozlov et al., 1983; Webster, 1986; Gammons and Barnes, 1989; Levin, 1994; Gammons and Williams-Jones, 1995a,b; Margolis and Britten, 1995; Spilsbury, 1995; Nokleberg et al., 1995; Gammons and Yu, 1997; Migdisov et al., 1999; Akinfiev and Zotov, 2001; Stefánsson and Seward, 2003). These studies have constrained the behavior of Ag in low-temperature aqueous fluids. Nonetheless, it is accepted that magmatic–hydrothermal fluids, evolved from silicate magma, are responsible for scavenging and transporting the silver (and other metals) from shallow level magma chambers (i.e., 4–10 km depth) upward to the epithermal and porphyry environments (Hedenquist et al., 1998; Redmond et al., 2004). In order to model quantitatively the behavior of silver across the continuum from the magma chamber to the porphyry and epithermal environments (and volcanic degassing), thermodynamic data constraining the behavior of silver over a range of *PT* conditions is required. Currently, however, there are no data that constrain the behavior of silver during the evolution of magmatic–hydrothermal fluids. Processes affecting the mass transfer of silver from the "parent" melt to an exsolved volatile phase (i.e., vapor, brine, supercritical fluid) control the absolute quantity of silver scavenged from a silicate melt and transported to the overlying environment where deposition occurs owing to changes in extensive and intensive parameters of the aqueous fluid. This study focuses on the behavior of silver at the *PT* conditions attending degassing of shallow-level (~4 to 6 km) felsic melt.

The genetic link between magmatic–hydrothermal fluids and shallow-level metal-rich ore deposits has been demonstrated in a plethora of field, analytical and experimental studies (Emmons, 1927; Sillitoe, 1979, 1989, 1993a,b, 2000; Burnham, 1979; Titley, 1981; Singer and Cox, 1986; Dilles, 1987 Richards et al., 1991; Vila and Sillitoe, 1991 Heinrich et al., 1992, 1999; Vennemann et al., 1993; Hedenquist and Lowenstern, 1994; Shinohara and Kazahaya, 1995; Thompson et al., 1995; Gammons et al., 1997; Shinohara and Hedenquist, 1997; Audétat et al., 1998, 2000 Hedenquist et al., 1998; Pettke et al., 2001; Muntean and Einaudi, 2001; Ulrich et al., 2001; Marschik and Fontboté, 2001; Frank et al., 2002; Requia et al., 2003; Rusk et al., 2004; Redmond et al., 2004; Halter et al., 2005; Rainbow et al., 2005; Camprubi et al., 2006a,b). Silicate melts exsolve an aqueous volatile phase owing to the attainment of H_2O saturation in the melt as a result of both decompression (first boiling) and crystallization (second boiling; Burnham, 1979). Data from natural and experimental fluid inclusion assemblages indicate that the composition of the volatile phase(s) exsolved a from upper crustal felsic silicate melts is dominated by chloride salts such as NaCl, KCl, $FeCl_2$, $CaCl_2$, etc. (Roedder, 1984; Audétat et al., 2000; Audétat and Pettke, 2003; Heinrich et al., 2003; Sirbescu and Nabelek, 2003; Simon et al., 2004; Candela and Piccoli, 2005). Thermodynamic studies of the phase relations in high-temperature aqueous fluids have concentrated on the *PT*–composition (*X*) relations in model systems such as NaCl–H_2O (Sourirajan and Kennedy, 1962; Henley and McNabb, 1978; Roedder, 1984; Bodnar and Sterner, 1985, 1987; Sterner and Bodnar, 1984; Bodnar et al., 1985; Anderko and Pitzer, 1993; Bodnar and Vityk, 1994), NaCl–KCl–H_2O (Roedder, 1984; Chou, 1987a; Chou et al., 1992; Sterner et al., 1988, 1992), NaCl–$CaCl_2$–H_2O (Vanko et al., 1988) and more complex fluids (Heinrich, 2007; Liebscher and Heinrich, 2007; Webster and Mandeville, 2007). Examination of the phase relations at magmatic *PTX* conditions indicates that a wide miscibility gap exists such that both vapor and brine coexist over much of the *PT* regime at which silicate melts evolve in Earth's upper crust. Data from natural fluid inclusion boiling assemblages demonstrate that silver is transported by both low- and high-salinity aqueous fluids in magmatic–hydrothermal systems (Audétat et al., 2000; Ulrich et al., 2001). Audétat et al. (2000) report up to several hundred μg/g silver in vapor and brine inclusions associated with ore mineralization in the Mole Granite, Australia. The fluid inclusions in their study exhibit homogenization temperatures (Th_{tot}) which range from 350 to 528 °C and the measured silver concentrations are greatest in brine inclusions which exhibit the highest Th_{tot} and salinity. One notable exception to this trend is a silver concentration of 590 μg/g in a low-density aqueous inclusion which contains 4.2 wt% NaCl equiv and has a Th_{tot} of 350 °C. Ulrich et al. (2001) report silver concentrations in boiling assemblages, trapped in minerals associated intimately with ore-stage mineralization at Bajo de la Alumbrera, Argentina, which suggest that silver partitions favorably into the brine; calculated Nernst-type partition coefficients for silver between vapor and brine, $D_{Ag}^{v,b}$, are on the order of 0.1 or lower. Homogenization temperatures reported for natural immiscible assemblages range from approximately 400–600 °C and, thus, these inclusions may be recording unmixing processes which may be unrelated to degassing from the ore-generative melt at depth. The apparent positive correlation between silver and salinity (i.e., wt% NaCl equiv) in natural aqueous fluid inclusions agrees with data for other transition metals (e.g., Au, Fe, Zn, Pb) from natural Audétat and Pettke, 2003) and S-free experimental studies (Holland, 1972; Candela and Holland, 1984; Williams et al., 1995; Frank et al., 2002; Simon et al., 2004, 2005). To date, there are no data, experimental or natural, which constrain the behavior of silver at magmatic conditions. However, experimental data collected at lower temperature do provide insight into the expected behavior of silver at the depositional stage of the magmatic–hydrothermal regime.

Data constraining the behavior of silver in low-temperature (i.e., <500 °C) aqueous fluids suggest that, depending on the pH and f_{HCl}/f_{H_2S} ratio of the aqueous fluid, silver solubility is dominated by either Ag–S complexes or Ag–Cl complexes (Akinfiev and Zotov, 2001). Seward (1976), based on experiments in a S-free assemblage, reports that $AgCl_n^{1-n}$ describes the stoichiometry of silver in S-free NaCl–H_2O vapor and that the ligand number, *n*, increases with temperature up to at least 353 °C, at saturated vapor pressure. Further, the coefficient *n* increases as total chlorinity of the volatile phase increases. The species $AgCl_2^-$ dominates silver speciation in aqueous vapor at temperatures from 277 to 353 °C (cf. Seward, 1976). Other studies

have examined the properties of silver in more complex NaCl–KCl–HCl–H_2O fluids (Levin, 1994; Gammons and Williams-Jones, 1995a,b; Akinfiev and Zotov, 2001). Data from these studies are consistent with $AgCl_n^{1-n}$ as the dominant silver-species in S-free fluids at temperatures up to 500 °C. Silver is a soft metal and is predicted to complex with bisulfide in a S-bearing volatile phase (Pearson, 1963). However, Wood et al. (1987) quantified experimentally the solubility of argentite (Ag_2S) in NaCl–H_2O–CO_2 aqueous solutions (0.5–5.0 M NaCl) from 200 to 350 °C and determined that Ag^0 and $AgCl_2^-$ dominate silver-speciation in the S-bearing NaCl–H_2O–CO_2 aqueous solutions. Stefánsson and Seward (2003) report that $AgHS^0$ is dominant and that with increasing pH silver-speciation is controlled by $Ag(HS)_2^-$ and $Ag_2S(HS)_2^{2-}$ at neutral to alkaline conditions at temperatures between 25 and 400 °C at saturated water vapor pressure and 50 MPa. The sum of all data constraining the behavior of silver in low-temperature aqueous fluids suggests that both Ag–Cl and Ag–S complexes are important in the redistribution of silver during processes associated with and driven by magmatism in Earth's upper crust. The critical need to develop a comprehensive model for silver mobility in the entire magmatic–hydrothermal regime is for data at magmatic conditions.

In this study, we report data from a rhyolite melt + vapor + brine + Ag^0 ± magnetite ± cerargyrite (AgCl) assemblage at 800 °C and pressures of 100 and 140 MPa. These conditions span the *PT* regime (i.e., 4–6 km depth) in which many silver-ore-generative magmatic–hydrothermal fluids evolve. They are consistent with data from natural fluid inclusion assemblages that demonstrate the evolution of ore-bearing aqueous fluids in many porphyry-ore systems from the causative magma at a depth on the order of 6 km. The data are presented as Nernst-type partition coefficients and apparent equilibrium constants for silver between vapor and brine, vapor and melt, and brine and melt.

2. PROCEDURES

2.1. Starting materials

The starting phase assemblage for all runs is provided in Table 1. A synthetic rhyolite minimum melt, $Qz_{0.38}Ab_{0.33}Or_{0.29}$ on an anhydrous basis at 100 MPa, was used in all experiments (Table 2). Aqueous solutions were prepared with reagent grade NaCl and KCl and aqueous HCl. The molar ratio of Na:K:H was set to unity in all starting aqueous solutions. The ratio of H to Na controls not only the pH of the aqueous fluid(s), but the extent of hydrolytic alteration. In this study, this ratio was set to unity to explore the effect of high HCl concentrations, hence high degrees of hydrolytic alteration, on metal partitioning. Future experiments will explore the effect of low HCl concentrations. Silver was added either as a 1:1 mixture of Ag:AgCl or as reagent grade elemental silver. Magnetite was added to two runs (19 and 22) to elucidate the silver-sequestering capacity of magnetite; these data are presented here, but are part of a larger study on crystal–melt equilibria being published separately.

Synthetic fluid inclusions were trapped either as glass-hosted fluid inclusions, formed as the melt cooled through the glass transition temperature (T_g), or as fluid inclusions in pre-fractured quartz cores (cf., Orville and Shelton, 1980 Sterner and Bodnar, 1984; Bodnar and Sterner, 1985, 1987; Bodnar et al., 1985). The glass-hosted fluid inclusions were present as discrete phases at run conditions prior to quenching and do not represent fluids formed during quench. Simon et al. (2007a) discuss extensively the ability to trap equilibrated aqueous fluids in pre-fractured quartz, owing to self-healing at run conditions, and glass, as the melt cools through the T_g. They conclude that both fluid-trapping techniques provide reasonable estimates of fluid solute loads at experimental conditions similar to those in the current study. Cores of natural quartz (Minas Gerais, Brazil) were cut to dimensions of approximately 1.5 cm length by 2- to 3-mm wide. The quartz cores were heated at 350 °C for 30 min and then fractured thermally by immersing them into a beaker of doubly-deionized, distilled water. The temperature to which the cores are heated is based on Sterner and Bodnar (1984) and Bodnar and Sterner (1985, 1987). Cores were kept at 120 °C until just prior to use and were allowed to come to room temperature before loading to prevent volatilization of the aqueous solution during the loading stage.

2.2. Experimental design

Bottom-welded platinum capsules (4.8 mm ID, 5 mm OD, 30 mm length) were loaded with rhyolite, 100 μL NaCl-, KCl- and HCl-bearing aqueous solution, powdered silver ± powdered AgCl ± magnetite crystals ± a quartz core as detailed in Table 1. Glass was loaded first followed by silver and cerargyrite to ensure that the latter two phases were not in contact with the platinum capsule. This was done to minimize direct contact between silver and platinum to prevent alloying of the two metals which would effectively reduce the activity of silver in the charge. Loaded capsules were immersed bottom down in dry ice and the capsule tops were welded shut. The capsules were then placed in a drying oven (120 °C) for 4 h, and maintenance of capsule mass (±3 mg) was used to verify the integrity of welded capsules. Capsules were placed inside René-41 cold-seal pressure vessels and pressurized to 50 MPa at room temperature. Pressure was imposed by a Haskell air-driven water-pressure intensifier and monitored with Bourdon-tube gauges (±2 MPa) calibrated against a factory-calibrated Heise gauge. The vessels were then heated to 800 °C with the pressure line left open. Once at 800 °C, pressure was raised to the desired run pressure. Temperatures were measured with type K (Chromel–Alumel) external thermocouples that were calibrated against internal thermocouples in the presence of the water-pressure medium for each experimental vessel.

An oxygen fugacity at approximately the nickel–nickel oxide (NNO) buffer was imposed by the composition of the experimental vessel (~53 wt% Ni) and the use of a buffer capsule containing elemental Ni and NiO placed behind the experimental charge (at the cold end of the charge) inside the pressure vessel. Following each run the presence

Table 1
Summary of experimental conditions

Run No.	P (MPa)	Run time (h)	Mass of haplogranite (g)	[a]Bulk salinity wt% NaCl equiv	Mass of Ag added (g)	Mass of AgCl added (g)	Mass of Mt added (g)	Quartz core added
4	140	206	0.04192	5.5	0.02130	0.02130	NA[c]	No
5	140	110	0.04334	5.5	0.01960	0.01960	NA	No
6	140	377	0.04398	5.5	0.02295	0.02295	NA	No
7	130[b]	205	0.04020	20	0.02057	0.02057	NA	No
14	140	160	0.04077	20	0.02269	0.02269	NA	No
19	100	117	0.04080	5.5	0.00850	NA[c]	0.04726	Yes
22	100	116	0.04118	1.8	0.00672	NA	NA	Yes
23	100	450	0.03980	1.8	0.00474	NA	0.04173	Yes
24	100	375	0.04054	1.8	0.00473	NA	NA	No
25	100	560	0.04098	5.5	0.00895	NA	NA	Yes

Replicate mass determinations of dry phases indicate that uncertainties in reported masses are no greater than 0.5%. One hundred microliters of aqueous solution was added to each run.

[a] This is the bulk salinity of the starting aqueous solution which contains equimolar quantities of NaCl, KCl and HCl.

[b] This run was stable at 140 MPa for 157 h, but it slowly bled in total pressure to 130 MPa over the last 48 h.

[c] NA, not added.

Table 2
Starting composition of synthetic rhyolite as determined by XRF (analysis performed by Activation Laboratories)

Oxide	Weight (%)
SiO_2	75.18
Al_2O_3	11.09
K_2O	4.43
Na_2O	3.67
CaO	0.17
Fe_2O_3	0.04
MnO	0.01
MgO	0.10
TiO_2	0.03
P_2O_5	0.03
LOI	4.51
Total	99.26

LOI, loss on ignition. From Lynton et al. (1993).

of both elemental Ni and NiO were noted in each buffer capsule. An $f_{O_2} \approx$ NNO is imposed via thermal dissociation of the water pressure medium, reaction of oxygen with the nickel pressure vessel and osmotic equilibration of hydrogen with the pressure medium and charge owing to the diffusion of hydrogen through the Pt capsule walls (Chou, 1987a). The f_{O_2} in experimental vessels was verified once during the study in each pressure vessel by using the hydrogen sensor technique (Ag–AgCl; H_2O–AgCl; Chou, 1987b); these experiments yielded $\log_{10} f_{O_2}$ values of -14 ± 1.0. To minimize variation of the intrinsic vessel f_{O_2} over the course of the experimental study, we mechanically abraded the interior of the vessel following each run by using a gun barrel brush to remove scaling and expose a clean vessel surface. The presence of both Ni and NiO in the buffer capsule after each run serves as evidence that each run was at an $f_{O_2} \approx$ NNO.

The hot end of each vessel was oriented in the furnace at a positive 10° angle from the horizontal lab bench to minimize the temperature gradient (Charles and Vidale, 1982). The temperature variation in all experiments is $\leqslant$5 °C along the length of the 3-cm capsule. The diameter of glass recovered from all runs is approximately 2 mm indicating that the temperature variation over the entire melt, at run conditions, is on the order of 0.4 °C. Quartz cores are 1.5 cm long and are located inside the capsule such that the quartz core lies across the hot spot. The temperature profile across the quartz core is about 799 °C at the cold end and 801 °C at the hot end. Thus, the temperature gradients are 1.7 °C/cm across the length of the capsule and 1.3 °C/cm across the length of the quartz core. This low thermal gradient minimizes the potential for quartz overgrowths; no overgrowths are recognized optically in the run products. The combination of a low-temperature gradient and tilted vessel position minimizes also the potential for thermally-induced convection gradients which, in turn, retards the premature healing of pre-fractured quartz chips (Simon et al., 2007a). The lack of premature healing is critical for trapping equilibrated aqueous fluids.

Experiments were quenched isobarically by using a compressed air stream from 800 to 200 °C followed by immersion in an ambient-temperature water bath. Capsules were removed from the vessels, cleaned with lab-grade H_2O and ethyl alcohol, examined optically and weighed to determine if the capsules remained sealed during the experiment. Only capsules that exhibited mechanical integrity, evinced by essentially no mass change, and yielded a strong hiss when pierced with a hypodermic syringe, evincing high internal capsule pressure, were processed for analysis.

2.3. Description of run products

All run products were examined petrographically to determine the stable phase assemblage upon quench. All capsules contained aqueous fluid at room temperature. In all runs, the melt quenched to a single bead of glass. Silver metal and cerargyrite were observed in runs 4 through 14 and only silver metal in runs 19 through 25; cerargyrite was not added to these latter runs. Fluid inclusions were

observed in both glass and quartz cores (Fig. 1). Low-density vapor fluid inclusions contain a vapor bubble surrounded by liquid and in some inclusions contain a small opaque particle. These particles are inferred to be elemental silver owing to their bright white color when viewed under reflected light. High-density brine fluid inclusions contain a vapor bubble, liquid, several salt crystals, typically one or more opaque particles, hypothesized to be silver based on their color when viewed under reflected light. The ratio of liquid to vapor in two-phase low-density vapor inclusions and the size of the vapor bubble are approximately constant in all runs. Magnetite was recovered from runs 19 and 22 indicating that it was a stable phase at run conditions. All run products are saturated in elemental silver and, thus, the measured concentrations represent the solubility of silver in all phases.

2.4. Analytical procedures

2.4.1. Analyses of experimental glasses

Glass samples were analyzed by using a JEOL JXA 8900 electron probe microanalyzer (EPMA) equipped with five wavelength dispersive spectrometers (WDS). The major element and Cl concentrations of run-product silicate glasses were quantified by using the following operating conditions: 15 keV accelerating potential, 5 nA beam current, and a 15-μm beam size with a minimum counting time of twenty seconds (sum of peak and background). Multiple line traverses were performed on each glass to evaluate the homogeneity of Cl and major elements. Following Morgan et al. (1996) and Acosta-Vigil et al. (2003), we performed several analyses to evaluate the effects of Na diffusion and concomitant Si and Al burn-in. No migration was observed during EPMA analyses. Standardization for Si, Al, Na and K was performed with a Yellowstone rhyolite (National Museum of Natural History, NMNH 72854 VG568). Kakanui hornblende was used to standardize iron. Scapolite (Meionite, Brazil, USNM R6600-1) was used to standardize chlorine. Detailed information for standards can be found in Jarosewich et al. (1980).

The concentration of silver in silicate glasses and fluid inclusions (described in Section 2.4.3) was quantified by using laser ablation inductively coupled plasma mass spectrometry (LA-ICPMS) with the setup described in Section 2.4.3. NIST-610 was used as the reference silicate glass. Absolute silver abundances were calculated by using the EPMA-determined Al_2O_3 concentration as the internal standard. NIST-610 is not a NIST certified silver standard; however, the NIST informative value of 254 μg/g agrees well with the globally accepted value of 239.4 ± 18.6 μg/g (1 standard deviation of the preferred average) as reported in Pearce et al. (1997). Thus, we suggest that NIST-610 can be used as a silver standard for the analysis of silicate glasses. In all runs, 4–8 large-beam (i.e., 60, 75, 80, 90 or

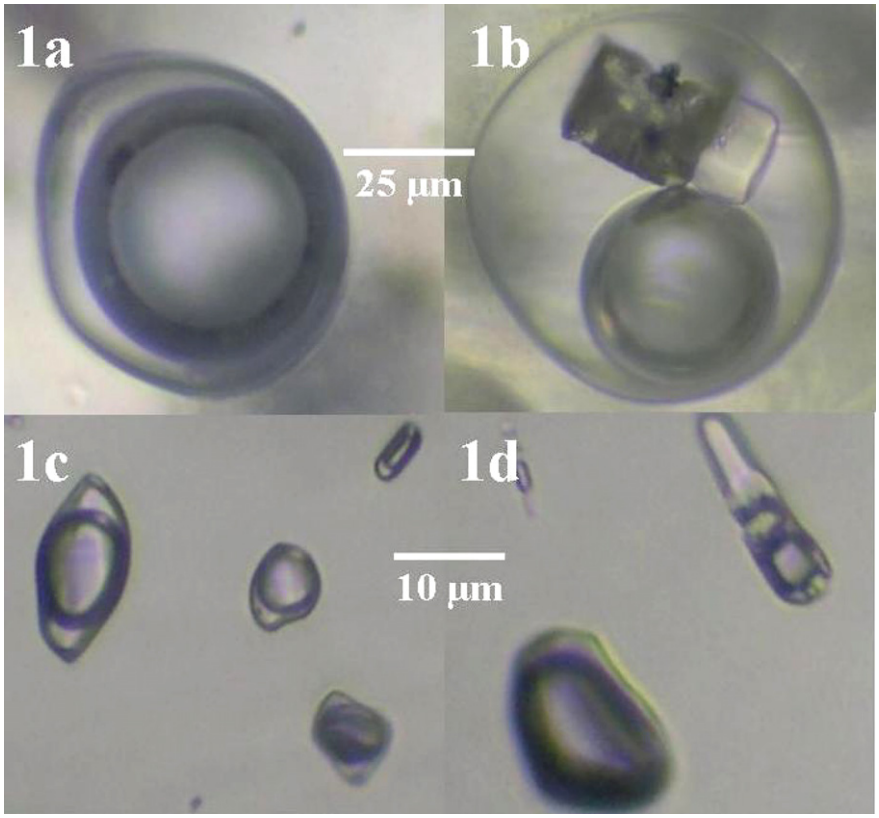

Fig. 1. Photomicrographs of synthetic fluid inclusions. (a) and (b) are vapor and brine, respectively, trapped at 100 MPa in silicate glass. (c) and (d) are vapor and brine, respectively, trapped at 100 MPa in pre-fractured quartz. Top scale bar is for (a) and (b). Bottom scale bar is for (c) and (d). All fluid inclusions in this figure were trapped in run 23.

100 μm spot size) analyses were performed on each glass. These glass analyses targeted multiple regions (i.e., core vs. rim) of each glass to elucidate potential gradients in the concentration of silver; no compositional gradients were detected. In addition to these large-beam analyses, the silver concentrations of glass volumes directly above and below analyzed fluid inclusions were quantified. Thus, the data reported here reflect 12–24 analyses per experimental glass. Transient analytical signals were integrated and isotope sensitivity ratios were calculated by using the NIST SRM-610 glass.

2.4.2. Absence of silver–platinum alloys

The phase diagram for the silver–platinum binary system indicates that silver and platinum form a single alloy $Ag_{15}Pt_{17}$ at temperatures from 400 to 803 °C at atmospheric pressure (Okamato, 1997). At temperatures at and above 803 °C a broad solvus exists extending from 30 at. % Ag and 93.9 at. % Pt at 803 °C to 40.0 at. % silver and 87.0 at. % platinum at 1188 °C. This indicates that silver and platinum are immiscible over this temperature range. Our experiments were performed with the center of the capsule at 800 °C and the hot and cold ends at 798 and 803 °C, respectively. To test whether alloying of silver and platinum occurred at run conditions, the capsule material from several runs was analyzed by energy dispersive spectrometry (EDS) EPMA. Silver was observed in some analyses, but was not ubiquitously distributed. Therefore, minimal to no alloying of silver and platinum appears to have occurred.

2.4.3. Fluid inclusion microthermometry

Following EPMA, the carbon coat was removed by diamond polishing and all probe mounts were cut into wafers on the order of 1 mm thick to expose glass on both sides. Quartz cores were mounted in epoxy and polished on both sides to permit optical examination and analysis of fluid inclusions. The quartz cores were mounted with the long axis parallel to the polished surface. This geometry allows us to analyze fluid inclusions along the length of the thermal gradient (1.7 °C/cm) to evaluate the homogeneity (i.e., bulk salinity expressed as wt% NaCl equiv) of trapped inclusions as discussed below. Fluid inclusions from multiple healed cracks along the length of the quartz core were analyzed. Variable salinities of fluid inclusions in either glass or quartz would indicate trapping on non-equilibrated aqueous fluids (cf. Krüger and Diamond, 2001). Individual fluid inclusions range in glass range in size from ~10–100 μm with the majority of fluid inclusions in the 10- to 30-μm range. Quartz-hosted fluid inclusions range in size from ~2–30 μm with the majority of inclusions in the 2- to 10-μm range. A USGS-type, gas-flow heating-freezing stage (Fluid, Inc.) was used to measure Tm_{ice} (final melting temperature of ice) and Td_{NaCl} (final dissolution temperature of NaCl; Bodnar and Vityk, 1994). The thermocouple was placed directly on top of the sample to prevent sample movement and to minimize the distance between the thermocouple and fluid inclusions; both serve to decrease uncertainties in temperature measurements. The heating-freezing stage was calibrated at −56.6 °C (pure CO_2 melting temperature), 0 °C (pure H_2O melting temperature) and 374.1 °C (pure H_2O critical temperature). Uncertainties in Tm_{ice} and Td_{NaCl} on the order of ±0.2 °C and ±1.5 °C, respectively, were estimated by performing replicate measurements on individual fluid inclusions.

2.4.4. LA-ICPMS analyses of fluid inclusions

The concentrations of silver, sodium, potassium and iron in individual fluid inclusions were quantified by LA-ICPMS using NBS-610 as the external standard and sodium as the internal standard, corrected to a true sodium concentration as described below. We analyzed fluid inclusions which yielded bulk salinities, expressed as wt% NaCl equiv, that were consistent with expected salinities based on known phase relations in the NaCl–KCl–$FeCl_2$–HCl–H_2O system. We analyzed quartz-hosted fluid inclusions from multiple healed cracks to evaluate the homogeneity of fluid inclusions across the quartz host (cf. Simon et al., 2007a). Glass-hosted fluid inclusions were also analyzed across the entire volume of glass to evaluate homogeneity. The use of Na as an internal standard has been evaluated previously (Heinrich et al., 2003; Simon et al., 2007a). Quadrupole ICPMS (Elan 6100, Perkin Elmer) settings were similar to those reported in Pettke et al. (2004). An energy-homogenized (Microlas) pulsed 193-nm ArF Excimer laser (Compex 102, Lamda Physik) was used to allow the controlled ablation of fluid inclusions and their host (Günther et al., 1997, 1998; Heinrich et al., 2003). The diameter of the laser beam was set slightly greater than the maximum diameter of each fluid inclusion such that the entire fluid inclusion was ablated together with a minimal volume of surrounding matrix glass. The transient signal is deconvoluted and processed to remove the addition of elements present in the host from the fluid inclusion signal interval such that the reported composition of the fluid inclusion represents only those elements contained in the fluid inclusion with no contribution from the host (cf. Heinrich et al., 2003). A dwell time of 10 ms was used for Si, Al, Na, K and Fe. The dwell time for silver was 20 ms. These short dwell times ensure representative sampling of the short, transient signals (Pettke et al., 2000), notably from glass-hosted inclusions. The transient signal for each analysis was integrated, and element ratios (e.g., Fe:Na) were quantified using a National Institute of Standards and Technology (NIST) SRM 610 silicate glass. Element ratios determined by LA-ICPMS were transformed into absolute element concentrations using sodium as the internal standard. Absolute concentrations of sodium in each fluid inclusion were determined by correcting the wt% NaCl equiv determined by microthermometry (Section 2.4.3.) for the presence of KCl, AgCl and $FeCl_2$ via the equation $NaCl_{true} = NaCl_{equiv} - 0.5 \times \Sigma X^{n+}Cl_n$ which assumes that all major cations in the fluid inclusion were present as chloride salts (Heinrich et al., 2003). The absence of sulfur in the experiments justifies this assumption. Note that element ratios, and hence partition coefficients, are independent of this assumption. Data reduction followed procedures outlined in Longerich et al. (1996) and Günther et al., 1997, 1998). The reported uncertainties for fluid inclusion and glass analyses represent the standard deviation of multiple analyses per experiment.

3. RESULTS

3.1. Composition of the rhyolite melt

3.1.1. Major element and chlorine concentrations in the melt

The major element, chlorine and silver concentrations of glasses are presented in Table 3. The consistent results across a range of run times from 111 to 560 h suggest that the melts reached equilibrium with respect to major elements and chlorine in less than 5 days, consistent with previous experimental studies (Carmichael and MacKenzie, 1963; Thompson and MacKenzie, 1967; Bailey et al., 1974; Bailey and Cooper, 1978; Baker and Rutherford, 1996; Gaillard et al., 2001; Scaillet and MacDonald, 2001; Clemente et al., 2004). The calculated aluminum saturation index (ASI = the molar ratio of $Al_2O_3/(Na_2O + K_2O)$) ranges from 1.19 to 1.31 indicates that all glasses are peraluminous. Most magmas associated with porphyry-ore deposits have ASI values which are below those of the melts in this study. Future experiments will be performed to evaluate the effect of ASI on silver partitioning. The decrease in the Na_2O concentration of the quenched melt, relative to the starting melt (Table 2), results from the exchange of Na in the melt for H in the volatile phases (vapor + brine). The concentration of K_2O does not change systematically which suggests that K_2O is not affected in a similar fashion to Na_2O. This effect has been documented in other studies of melt–volatile phase equilibria (Frank et al., 2002). EPMA glass totals on the order of 94–96 wt% are consistent with the expected water solubility of 4–6 wt% in rhyolite melt at 100–150 MPa (McMillan and Holloway, 1987).

3.1.2. Silver solubility in rhyolite melt and processing signals in light of the metal nugget controversy

The concentrations of silver in silicate glasses (Table 3) exhibit more variability than major elements and chlorine. The low and high silver concentration ($\pm 2\sigma$ of the mean) at 140 MPa are 322 (94) μg/g and 1250 (170) μg/g yielding an average of 322 (94) μg/g. The low and high silver concentration ($\pm 2\sigma$) at 100 MPa are 40 (9) μg/g and 228 (74) μg/g yielding an average of 105 ± 21 μg/g. Each LA-ICPMS transient signal was evaluated critically for the presence of silver nuggets (cf. Borisov and Palme, 1997; Ertel et al., 1999; Fortefant et al., 2003; Cottrell and Walker, 2006; Simon et al., 2007b) and their presence was detected in approximately 5–10% of all analyses. Including the silver nuggets in the signal invariably results in a higher silver concentration and, thus, the origin of the nuggets and whether or not to include or remove them during signal processing is critical not only for the determination of silver solubility in the melt, but for the calculation of partition coefficients and equilibrium constants.

The silicate melt in all runs was in intimate contact with a silver source and at run conditions this silver diffused into and through the melt until the melt reached silver saturation. To calculate the approximate time required for the melt to reach silver saturation via diffusion, note that the small thermal gradient should minimize if not eliminate convection in the melt, we estimated a reasonable diffusivity

Table 3
Concentrations of major elements (EPMA), Cl (EPMA) and Ag (LA-ICPMS) in the run product glasses

Run No.	P (MPa)	SiO_2 wt% ($\pm 2\sigma$)	K_2O wt% ($\pm 2\sigma$)	Na_2O wt% ($\pm 2\sigma$)	FeO wt% ($\pm 2\sigma$)	Al_2O_3 wt% ($\pm 2\sigma$)	Cl wt% ($\pm 2\sigma$)	Ag μg/g ($\pm 2\sigma$)	Total	ASI
4	140	76.10 (0.90)	3.93 (0.20)	2.80 (0.13)	0.05 (0.05)	11.57 (0.44)	0.16 (0.01)	588 (115)	94.57 (0.36)	1.31
5	140	76.45 (0.53)	3.77 (0.09)	2.73 (0.07)	0.03 (0.03)	11.14 (0.24)	0.14 (0.01)	870 (100)	94.23 (0.33)	1.30
6	140	75.87 (0.55)	3.88 (0.05)	3.05 (0.11)	0.04 (0.03)	11.90 (0.36)	0.11 (0.01)	1250 (170)	94.82 (0.58)	1.29
7	130	76.35 (0.29)	4.98 (0.09)	2.24 (0.10)	0.05 (0.03)	11.43 (0.14)	0.14 (0.01)	322 (94)	95.17 (0.33)	1.26
14	140	75.69 (0.37)	4.85 (0.13)	2.39 (0.14)	0.04 (0.05)	11.23 (0.34)	0.16 (0.01)	343 (86)	94.33 (0.56)	1.22
Mean		76.09 (0.16)	4.28 (0.15)	2.64 (0.08)	0.04 (0.01)	11.45 (0.08)	0.14 (0.01)	675 (98)	94.62 (0.10)	
19	100	75.34 (0.52)	4.15 (0.21)	3.02 (0.07)	0.29 (0.09)	11.36 (0.28)	0.14 (0.01)	59 (17)	95.87 (0.47)	1.24
22	100	75.29 (0.61)	3.92 (0.13)	3.32 (0.13)	0.54 (0.24)	11.38 (0.31)	0.13 (0.01)	228 (74)	94.27 (0.43)	1.20
23	100	75.66 (0.50)	4.18 (0.14)	3.37 (0.09)	0.04 (0.03)	11.31 (0.25)	0.15 (0.01)	40 (9)	94.55 (0.46)	1.24
24	100	75.40 (0.51)	4.13 (018)	3.24 (0.15)	0.04 (0.03)	11.23 (0.32)	0.05 (0.01)	93 (34)	94.68 (0.44)	1.19
25	100	74.67 (0.58)	4.54 (0.20)	3.04 (0.10)	0.04 (0.02)	11.69 (0.32)	0.16 (0.01)	103 (31)	94.10 (0.43)	1.22
Mean		75.27 (0.10)	4.18 (0.06)	3.20 (0.05)	0.19 (0.06)	11.39 (0.05)	0.13 (0.01)	105 (21)	94.69 (0.20)	

Uncertainties are presented as twice the standard error of the mean ($\pm 2\sigma$) for the replicate measurements. Each EPMA datum represents the average of a minimum of 10 spot analyses in different areas of a given experimental glass. The Ag concentrations represent the average of large spot sizes (75 or 90 μm) which were used to ablate glass volumes which contained no fluid inclusions and also the glass volumes directly above and below ablated glass-hosted fluid inclusions. The Aluminum saturation index (ASI) was calculated as the molar ratio $[Al_2O_3/(Na_2O + K_2O)]$; the concentration of Ca in the starting glass is 0.17 wt% Lynton et al. (1993) and was not analyzed for in run products. The calculated values of ASI indicate that all experimental melts were peraluminous.

for silver in haplogranite by using diffusion data for sodium and cesium in haplogranite melts at 800 °C. Watson (1994) reports diffusion coefficients of approximately $10^{-9.5}$ m^2 s^{-1} and 10^{-12} m^2 s^{-1} for univalent sodium and cesium, respectively. Univalent silver has a radius (0.126 nm) that is approximately halfway between that of sodium (0.095 nm) and cesium (0.169 nm) and, thus, a reasonable estimate for the diffusion coefficient of silver is 10^{-11} m^2 s^{-1}. Using a diffusion coefficient for silver of 10^{-11} m^2 s^{-1} and a melt diameter of 2 mm, the calculated timescale for diffusional equilibration of silver in the melt is approximately 110 h. Note that silver is also transported via the vapor to the vapor–melt interface; thus, the calculated time is a maximum. Based on the homogeneity of major elements and chlorine in the silicate glass and run durations of 110–560 h, the melt should contain a homogeneous distribution of silver at run conditions.

Two hypotheses can be put forth to explain the presence of silver nuggets in silicate glasses in the present study: (1) the silver nuggets existed as discrete silver particles (Ag^0) which were present at run conditions; and (2) silver was homogeneously dissolved in the melt at run conditions and the silver nuggets formed during quench owing to decreased silver solubility in the melt with decreasing temperature. The first hypothesis is based on the experimentally-determined relationship between metal solubility in silicate melts and oxygen fugacity. Ertel et al. (1999) present and discuss solubility data for platinum metal in haplobasalt and conclude that metal solubility is a function of f_{O_2}. Their results and those from Borisov and Palme (1997) and Fortefant et al. (2003) indicate that platinum solubility in haplobasalt decreases from approximately 1×10^4 ng/g to 1×10^1 ng/g (three orders of magnitude) as log f_{O_2} decreases from 0 to −6 (six orders of magnitude). Ertel et al. (1999) attribute the observed scatter in a linear regression of platinum concentration vs f_{O_2} to the presence of platinum micronuggets in the quenched melt (i.e., glass). If their hypothesis is correct, then metal nuggets observed in LA-ICPMS transient signals should not be included during data reduction.

The second hypothesis to explain the origin of metal nuggets in experimental glasses has been discussed by Cottrell and Walker (2006). They quantified experimentally the solubility of platinum in basalt and presented back-scattered electron (BSE) images of the run product glasses which show the presence of platinum nuggets in the recovered basalt glass. The nuggets in their glasses range in diameter from 50 nm to 2 μm. Cottrell and Walker (2006) attribute the nuggets to the expected rapid decrease in platinum solubility in the basalt melt as the run is quenched. If this second hypothesis is correct, then metal nuggets observed in LA-ICPMS transient signals should be included during data reduction. Thus, a conundrum exists with respect to the treatment of LA-ICPMS data which display evidence for the presence of metal nuggets.

The experimental charges in the present study were initially at atmospheric f_{O_2}. Once the experiment reaches the desired run conditions, it takes on the order of 24 h for hydrogen diffusion to establish osmotic equilibrium between the charge and the vessel and reach the desired final $f_{O_2} \approx$ NNO (Chou, 1987b). Thus, based on the results discussed in Ertel et al. (1999), it is expected that the ability of silver to dissolve into the silicate melt is greatest over this first day. As the f_{O_2} decreases to its final equilibrium value of $f_{O_2} \approx$ NNO, the solubility of silver should decrease, if the same relationship holds for silver as for platinum in the basalt melts, resulting in the precipitation of silver nuggets in the melt. The size of these nuggets is presumed to remain small enough (cf. Cottrell and Walker, 2006) that the nuggets remain neutrally buoyant in the melt for the duration of the run and, thus, are observed in the LA-ICPMS signals. We examined glasses for the presence of micronuggets by using BSE imaging and observed no silver nuggets even though, based on the laser ablation rate during LA-ICPMS analysis, the diameter of the silver nuggets in some signals should have approached several microns. This is attributed to the fact that glass-hosted nuggets observed in the present study were located at least several microns beneath the glass surface, determined from the amount of time required to ablate into the glass before a nugget is observed in the transient signal. In the 5 to 10 % of all LA-ICPMS signals in this study which display evidence for the presence of a silver nugget, manually removing the silver nugget(s) from the single transient glass signal results in a decrease in the calculated silver concentration of the melt of at most one order of magnitude. This is less than the third order of magnitude concentration variation observed for platinum in the Ertel et al. (1999) study. However, the results reported here do not falsify their hypothesis in light of the fact that the melt would not have reached diffusional equilibrium with silver during the initial 24 h period required to establish the desired f_{O_2} as the f_{O_2} of the charge was continually decreasing to the final value of $f_{O_2} \approx$ NNO. In this case, based on the diffusion length scale over the first 24 h, one might expect to see a greater density of nuggets near the outer portion of a glass bead relative to the center of the glass bead. We did not observe this in any run-product glass.

To address hypothesis two, we calculated the hypothetical diameter of a silver nugget which may form during quench. The experiments in this paper were quenched from 800 to 400 °C over a total time of 35–40 s, resulting in a quench rate of approximately 10 °C s^{-1} through the T_g. Using a reasonable silver diffusivity in haplogranite of 10^{-11} m^2 s^{-1} and a time of 40 s for the melt to cool to the T_g yields a diffusion distance of 20 μm. Thus, a silver particle could scavenge silver from a spherical volume of approximately 3.2×10^4 $\mu m^3 (4 \times x^3$ with $x =$ diffusion length) during quench, admittedly assuming unrealistically that the diffusivity remains constant. This should result in the growth of a silver nugget on the order of several microns, assuming a single nucleation site and growth of this one nugget, consistent with the size of the particles observed in LA-ICPMS signals in the present study. This model calculation is consistent with a quench origin for the obersved silver nuggets. Thus, data in the present study can not be used to falsify either hypothesis for the formation of metal nuggets in silicate melt.

We suggest that both hypotheses may be correct; however, this would require the ability to determine the proportion of silver in each nugget present as a stable phase at run conditions and the proportion which was added to the nugget (i.e., nucleation site) during quench. Analysis of all transient signals in this study indicates that the higher silver concentrations in silicate glasses within and among individual runs do not correspond to a disproportionate number of silver nuggets in the glass; i.e., there is no correlation between the number of silver nuggets in silicate melt and the reported concentration of silver in the melt. Manually removing a silver nugget from a transient glass signal results in a decrease in the calculated silver concentration of the melt of up to one order of magnitude. Retaining all silver nuggets during signal processing increases the final calculated average silver concentration of the melt by less than 10%. For example, the silver concentrations in silicate glass from run 19 vary from 32 to 84 μg/g with a mean concentration of ($\pm 2\sigma$) 59 ± 17 μg/g. The mean silver concentration represents the average of 12 LA-ICPMS glass analyses on the single glass bead recovered from the run. Six LA-ICPMS analyses were performed using a 75-μm laser spot size while the other analyses used spot sizes varying from 35 to 60 μm. There are no observed statistical differences in silver concentrations and laser diameter. Silver nuggets were observed in one transient signal from this glass and removing the silver nugget results in a decrease in the average silver concentration that is within the 2σ reported in Table 3. As such, in the absence of conclusive evidence that the entire mass of each silver nugget was a stable phase at run conditions, we have included all nuggets during signal processing. While this may overestimate slightly the true silver solubility in felsic melt, it is the statistically honest approach. This results in an underestimation of the calculated vapor/melt and brine/melt partition coefficients, hence the modeling results presented below place a minimum on the silver-scavenging ability of both vapor and brine.

3.2. Major and trace element concentrations in vapor and brine

The concentrations of sodium, potassium, iron and silver in glass- and quartz-hosted aqueous vapor and brine fluid inclusions are listed in Tables 4 and 5, respectively. Major element concentrations and bulk salinities in all runs agree with published phase relations in the NaCl–KCl–$FeCl_2$–H_2O system and previous experimental studies at similar conditions (Frank et al., 2002; Simon et al., 2004, 2005, 2006, 2007b). There are no systematic data on the effect of cerargyrite on phase relations in the NaCl–KCl–$FeCl_2$–H_2O system. Krüger and Diamond, 2001 report that saturating a 6-wt% NaCl equiv CO_2–H_2O–NaCl fluid with cerargyrite depresses Th by ±2–3 °C from the Th value expected from a chlorargyrite-free CO_2–H_2O–NaCl fluid. This translates into a change in salinity of 0.5 wt% NaCl equiv. A change of 0.5 wt% NaCl equiv (e.g., from 45 to 44.5 NaCl equiv) changes the silver concentration in a brine inclusion by 1.2%. Changing the salinity of a low-density vapor by 0.5 wt% NaCl equiv changes the concentration of silver in the vapor by 4.5%. Based on the data presented in Krüger and Diamond (2001) and our microthermometric measurements we suggest that the presence of chlorargyrite in both vapor and brine does not modify significantly the experimental estimate for the position of the solvus in the NaCl–KCl–$FeCl_2$–H_2O system (See Table 5).

The molal ratios ($\pm 2\sigma$) of sodium to potassium in vapor and brine at 100 MPa are 3.7 ± 0.4 and 2.5 ± 0.2, respectively and at 140 MPa are 2.5 ± 0.3 and 1.9 ± 0.2, respectively. The increase in the Na/K ratio of the aqueous fluids reflects the exchange of sodium in the melt for hydrogen and potassium in the starting aqueous solution. Fig. 2a shows the transient analytical signal for a typical glass hosted fluid inclusion wherein the intensity for sodium, potassium and silver all parallel one another and rise and fall over the same time interval. The presence of anomalous jumps in silver intensity was noted in some transient glass signals for vapor and brine analyses. We interpret these jumps to represent the entrapment of silver micro-nuggets (Borisov and Palme, 1997; Ertel et al., 1999; Fortefant et al., 2003; Cottrell and Walker, 2006) in the fluid inclusion during quench. Silver concentrations from such anomalous inclusions were not included in the average concentrations used to calculate partition coefficients and equilibrium constants. The concentration ($\pm 2\sigma$) of silver in vapor ranges from 1.2 (0.1) mg/g to 5.1 (0.7) mg/g and from 7.0 (2.6) mg/g to 30.7 (20.0) mg/g at 140 MPa. These data suggest that the solubility of silver in vapor increases with increasing pressure and salinity of the aqueous fluid. Likewise, the concentration ($\pm 2\sigma$) of silver in brine ranges from 83.8 (26.6) mg/g to 112.9 (8.1) mg/g and from 161.4 (8.8) mg/g to 491.0 (51.1) mg/g at 140 MPa. It should be noted that the concentrations of silver in some glass- and quartz-hosted vapor fluid inclusions differ by as much as a factor of two; however, we suggest that the data constrain well the solubility of silver at the reported experimental conditions (see Figs. 3–5).

3.3. Fugacity and concentration of HCl

The fugacity of HCl, f_{HCl}, was buffered in the runs at 140 MPa owing to saturation with elemental silver and silver chloride. The f_{HCl} can be described by the equilibrium

$$Ag^0 + HCl^{mvp} = AgCl^{mvp} + 0.5H_2 \quad (1)$$

where mvp stands for magmatic volatile phase. The activities of Ag^0 and AgCl are unity and the value for f_{H_2} is 6.2 bars at 140 MPa; f_{H_2} was calculated by using equations of Huebner and Sato (1970) and Belonoshko et al. (1992). These data yield a value for f_{HCl} equal to 4.1. The fugacity of water, f_{H_2O}, at 140 MPa is 1147 bars and the molar ratio of HCl to H_2O, according to the Lewis and Randall rule, is 4×10^{-3} yielding a calculated log HCl concentration (wt. %) in the vapor at 140 MPa of 4. The value for the equilibrium constant for Eq. (1) is 0.6. The lower pressure runs did not contain AgCl. To calculate the concentration of HCl in volatile phases at 100 MPa and brine at 140 MPa, we followed Williams et al. (1997) and used their equation:

Table 4
LA-ICPMS data ($\pm 2\sigma$) for S-free vapor fluid inclusions and melt

Run No.	P (MPa)	Type of inclusion	Number[a] of inclusions analyzed	Matrix[b]	Bulk[c] wt% NaCl equiv	Final[d] wt% NaCl equiv	HCl[e] mg/g ($\pm 2\sigma$)	Na mg/g ($\pm 2\sigma$)	K mg/g ($\pm 2\sigma$)	Fe mg/g ($\pm 2\sigma$)	Ag mg/g ($\pm 2\sigma$)
4	140	Vapor	11	Glass	20	8.3–8.9	42.8 (8.2)	25.0 (1.6)	17.0 (1.8)	NA[h]	19.5 (8.3)
5	140	Vapor	8	Glass	20	8.5–9.7	42.6 (4.2)	25.0 (2.2)	13.0 (1.8)	NA[h]	23.1 (8.6)
6	140	Vapor	8	Glass	20	9.1–9.4	38.6 (3.9)	22.0 (4.3)	12.5 (3.0)	NA[h]	30.7 (20.0)
7	140	Vapor	7	Glass	20	8.7–9.3	28.7 (9.9)	24.0 (1.2)	14.0 (4.0)	NA[h]	7.0 (2.6)
14	140	Vapor	8	Glass	20	8.5–9.3	25.6 (9.0)	24.5 (1.6)	23.0 (1.9)	NA[h]	10.5 (4.4)
19	100	Vapor	3	Quartz	5.5	1.3–2.1	7.1 (1.3)	5.2 (1.0)	4.1 (0.7)	1.9 (1.2)	2.1. (0.33)
19	100	Vapor	1	Glass		1.4–1.9		5.6 (1.3)	2.9 (0.5)	1.0 (0.6)	1.8 (0.30)
22	100	Vapor	10	Quartz	1.8	1.4–1.9	3.5 (0.6)	2.4 (0.7)	2.2 (0.5)	NA[h]	5.0 (1.2)
22	100	Vapor	2	Glass		1.5–2.0		4.53 (0.2)	2.2 (0.1)		2.5 (0.6)
23	100	Vapor	4	Quartz	1.8	1.6–2.2	3.2 (0.9)	4.8 (0.5)	3.1 (1.1)	2.4 (1.0.)	2.5 (0.5)
23	100	Vapor	4	Glass		1.3–2.1		5.0 (0.05)	2.9 (0.4)	3.2 (0.09)	1.2 (0.1)
24	100	Vapor	14	Glass	1.8	1.4–2.0	15.6 (0.5)	6.1 (0.5)	1.7 (0.8)	NA[h]	3.3 (0.8)
25	100	Vapor	7	Quartz	1.8	1.4–2.2	4.4 (0.9)	3.8 (0.2)	2.6 (0.3)	NA[h]	2.8 (0.2)
25	100	Vapor	3	Glass		1.5–2.1		5.4 (0.5)	2.2 (0.2)		5.1 (0.7)

[a]This column provides the total number of inclusions analyzed by LA-ICPMS.
[b]This is the matrix from which the fluid inclusions were liberated.
[c]This is the bulk salinity of the initial starting aqueous solution.
[d]This is the final range of salinities, expressed as wt% NaCl equiv.
[e]HCl concentrations calculated following Williams et al. (1997).
[f]NI, none identified: the bulk salinity of these runs lies just inside the solvus of the NaCl–KCl–H_2O model system; however, brine inclusions were not found.
[g]NS, none suitable: several glass-hosted brine inclusions were identified; however, their significant depth inside the glass matrix prevented us from analyzing them during the analytical session.
[h]NA, not added to the experiment.

Table 5
LA-ICPMS data (±2σ) for S-free brine fluid inclusions and melt

Run No.	P (MPa)	Type of inclusion	Number[a] of inclusions analyzed	Matrix[b]	Bulk[c] wt% NaCl equiv	Final[d] wt% NaCl equiv	HCl[e] mg/g (±2σ)	Na mg/g (±2σ)	K mg/g (±2σ)	Fe mg/g (±2σ)	Ag mg/g (±2σ)
4	140	Brine	9	Glass		41–44	73.6 (1.3)	79.5 (11.0)	66.0 (10.0)	NA[h]	265.8 (58.5)
5	140	Brine	7	Glass		42–46	68.5 (1.1)	77.0 (8.4)	55.0 (7.5)	NA[h]	325.7 (55.5)
6	140	Brine	8	Glass		42–44	47.9 (1.2)	84.0 (29.0)	47.0 (27.0)	NA[h]	491.0 (51.1)
7	140	Brine	4	Glass		42–44	42.6 (2.5)	90.5 (2.0)	114.0 (31.0)	NA[h]	163.0 (17.0)
14	140	Brine	8	Glass		41–43	36.0 (2.4)	87.5 (3.4)	98.0 (9.7)	NA[h]	161.4 (8.8)
19	100	Brine	3	Quartz		61–67	87.8 (1.8)	153 (16.7)	92.4 (12.4)	88.6 (24)	83.8 (26.6)
19	100	Brine	NI[f]	Glass							
22	100	Brine	NI[f]	Quartz						NA[h]	
22	100	Brine	NI[f]	Glass							
23	100	Brine	8	Quartz			48.2 (2.8)	164.5 (15.2)	136.1 (32.4)	13.1 (10.5)	85.6. (19.0)
23	100	Brine	NS[g]	Glass							
24	100	Brine	NI[f]	Glass						NA[h]	
25	100	Brine	7	Quartz		63–68	66.1 (2.8)	153.7 (2.9)	134.1 (3.9)	NA[h]	112.9 (8.1)
25	100	Brine	NI[f]	Glass							

See Table 4 caption for footnotes. [f]NS, brine inclusions in this glass were identified, but not analyzed owing to its considerable depth.

$$\log \frac{NaCl^{mvp}}{HCl^{mvp}} = \log \frac{1}{K_{H/Na}^{mvp/m}} \times \frac{C_{Na}^{m}}{\sum Alkalies^{melt}(ASI-1)}, \quad (2)$$

where mvp stands for magmatic volatile phase, ASI is the aluminum saturation index of the melt (i.e., the molar ratio $Al_2O_3/(Na_2O + K_2O)$) and $K_{H/Na}^{mvp/m}$ is defined as

$$K_{H/Na}^{mvp/m} = \frac{(C_H^{mvp} \times C_{Na}^{melt})}{(C_H^{melt} \times C_{Na}^{mvp})} \quad (3)$$

(Holland, 1972). Model values for $K_{H/Na}^{mvp/m}$ were taken from Williams et al. (1997). The calculated log HCl concentrations (wt%) in vapor and brine are 3.7 and 4.8 at 140 MPa, respectively. At 100 MPa, the average HCl concentrations in vapor and brine are 3.7 and 4.8 μg/g, respectively The calculated HCl concentrations and the increase in the aluminum saturation index (ASI) of the melt to >1.19 from the starting value of 1.00 agree with the model presented in Candela (1990) which hypothesized that highly peraluminous silicate melts should evolve and be in equilibrium with HCl-rich aqueous fluids.

3.4. Silver concentration in magnetite

The concentration of silver in magnetite crystals recovered from experiments 19 and 23 was determined by LA-ICPMS. Analyses were calibrated externally by using the NIST SRM 610 silicate glass standard (Heinrich et al., 2003; Simon et al., 2003). The absolute concentration of silver in magnetite was calculated by using the stoichiometric concentration of iron in end-member magnetite; no elements (e.g., titanium) were present which could have formed a solid-solution with magnetite. The measured concentrations of silver range from below detection limit (Longerich et al., 1996) to 0.16 μg/g. Based on the fact that the majority of the analyses yielded concentrations below the LOD, we suggest that a value of 0.01 μg/g represents an upper bound for the solubility of silver in magnetite at the experimental conditions described herein.

3.5. Demonstration of equilibrium

Equilibrium was evaluated by noting the invariance of calculated Nernst-type partition coefficients as a function of run time and also by evaluating the homogeneity of fluid inclusion salinities throughout the charge. The partitioning behavior of silver between vapor and brine, vapor and melt, and brine and melt remains relatively constant over run durations varying from 111 to 560 h as shown in Figs. 3–5. The time invariance of the partitioning data is inferred to reflect the achievement of equilibrium in agreement with previous experimental studies (Giggenbach, 1975, 1992; Candela and Holland, 1984; Webster, 1992; Gammons and Williams-Jones, 1995a,b; Gammons and Yu, 1997; Gammons et al., 1997; Jugo et al., 1999; Archibald et al., 2002a,b; Frank et al., 2002; Simon et al., 2004, 2005, 2006, 2007a,b; Repel et al., 2006; Zezin et al., 2007). The synthetic fluid inclusions have bulk salinities which agree with predictions based on extant data (Sourirajan and Kennedy, 1962; Henley and McNabb, 1978; Roedder, 1984; Bodnar and Sterner, 1985; Sterner and Bodnar,

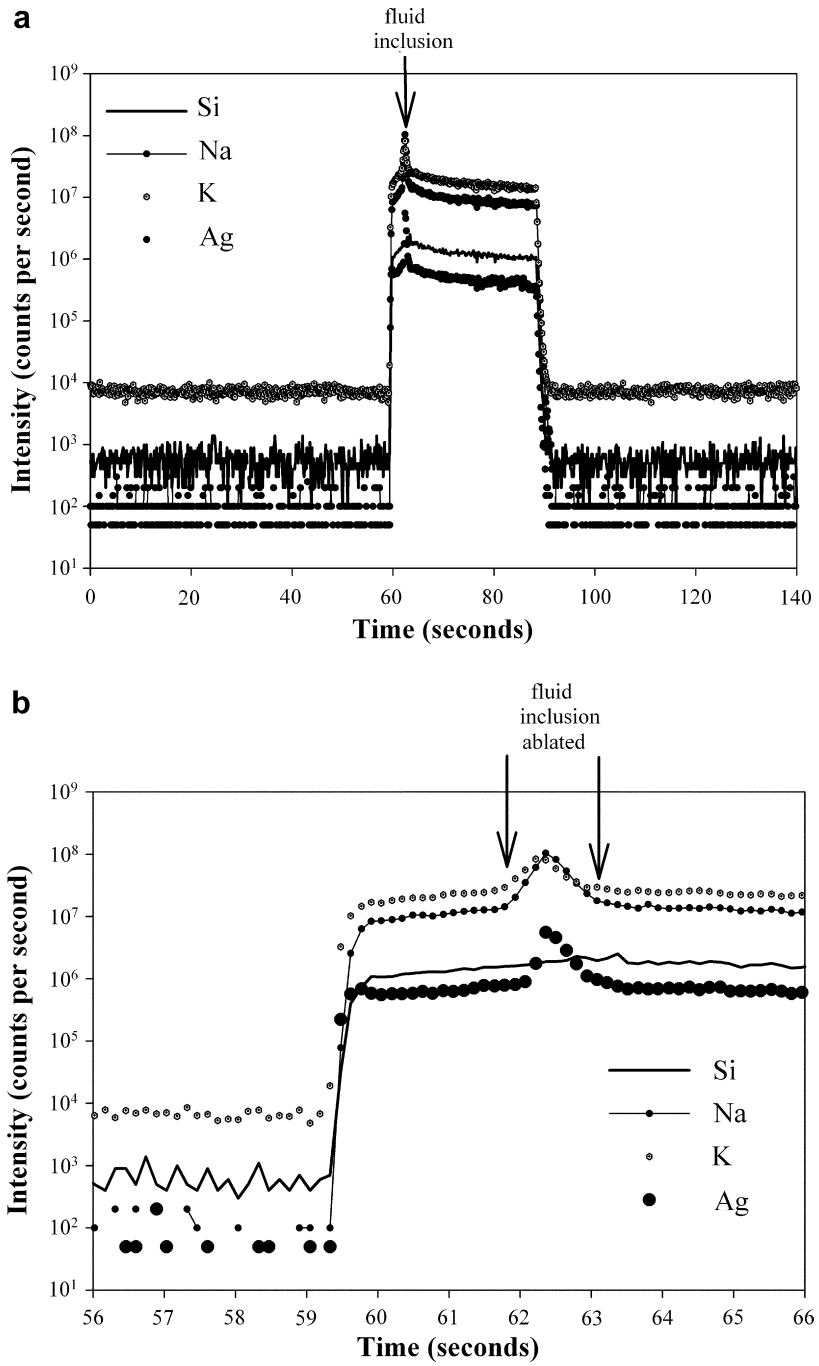

Fig. 2. (a) LA-ICPMS transient signal of a glass-hosted fluid inclusion analysis. Gas background is analyzed from 0 to 60 s at which time the laser is turned on and the glass ablation begun. The ablation interval is highlighted in (b). The signals for other elements (Al and Fe) have been omitted for clarity. (b) The signal from (a) focusing only on the time interval for the fluid inclusion ablation and glass above and just below the fluid inclusion. The signal for silver parallels those of sodium and potassium indicating that the silver is contained within the ablated fluid inclusion. The concentration of silver in the fluid inclusion was calculated by subtracting the average concentration (counts per second) of silver in the fluid interval from 61.8 to 63.3 s from the concentration (counts per second) of silver in the glass calculated from the interval from 64 to 88 s and using the microthermometrically determined sodium concentration of the fluid inclusions as described in the text.

1984; Bodnar et al., 1985; Bodnar and Sterner, 1987; Bodnar et al., 1985; Anderko and Pitzer, 1993; Bodnar and Vityk, 1994), NaCl–KCl–H_2O (Roedder, 1984; Chou, 1987a; Chou et al., 1992; Sterner et al., 1988, 1992). No salinity gradients were observed in fluid inclusions trapped either in glass or quartz; this is consistent with the low thermal gradient across the charge. The consistent salinities of all vapor and brine fluid inclusions and the consistent partition coefficients are interpreted to suggest that equilibrium was attained and preserved in quenched run products in all experiments.

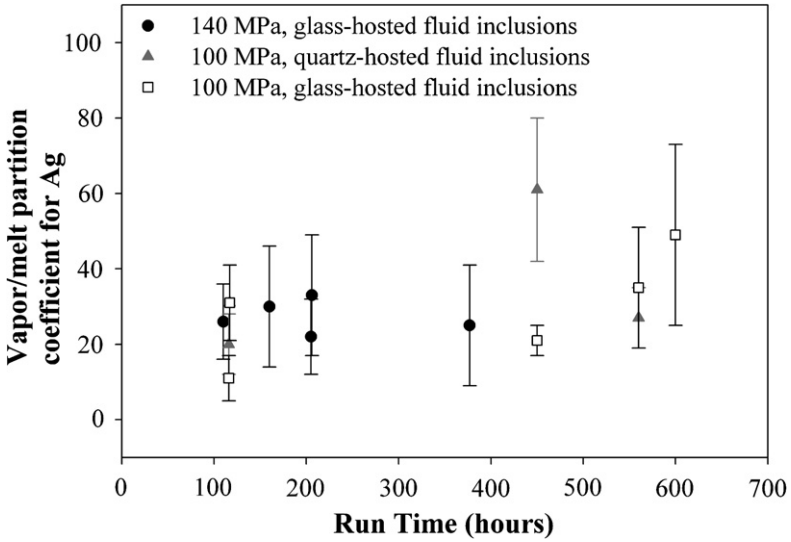

Fig. 3. The experimentally-determined partition coefficients for silver between coexisting vapor and melt as a function of run duration at 800 °C and $f_{O_2} \approx$ NNO. Uncertainties represent twice the standard error of the mean.

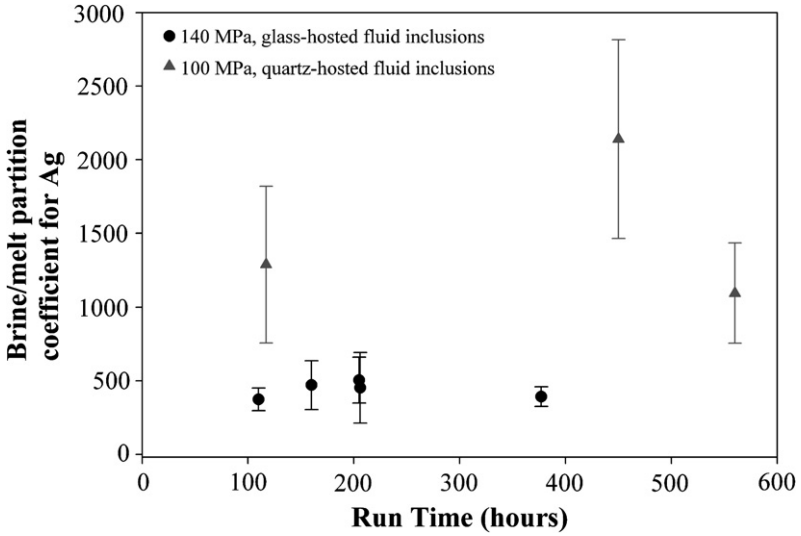

Fig. 4. The experimentally-determined partition coefficients for silver between coexisting brine and melt as a function of run duration at 800 °C and $f_{O_2} \approx$ NNO. Uncertainties represent twice the standard error of the mean.

4. DISCUSSION

4.1. The effect of pressure on silver solubility in melt, vapor and brine

The measured silver concentrations in rhyolite glass suggest that pressure affects the solubility of silver in silicate melt at 800 °C. The most likely cause for the observed behavior of silver with pressure is the change in the water content of the melt. As pressure decreases from 140 to 100 MPa, water solubility in the melt decreases and the melt becomes more polymerized (Mysen, 1991). As melt polymerization increases, the chemical potential of silver in the melt increases and this enhances the partitioning of silver from the melt to an exsolved aqueous phase. This behavior has also been observed for copper (Williams et al., 1995).

In order to evaluate the relationship between Na and Ag, apparent exchange constants were calculated as

$$K^{i/m}_{Ag,Na} = \frac{C^{i}_{Ag} * C^{m}_{Na}}{C^{m}_{Ag} * C^{i}_{Na}} \quad (4)$$

where i stands for vapor (v) or brine (b) and m represents melt. These data are presented in Table 6 The average values for $K^{v/m}_{Ag,Na}(\pm 2\sigma)$ at 100 and 140 MPa are 105 ± 68 and 14 ± 6. The average values for $K^{b/m}_{Ag,Na}(\pm 2\sigma)$ at 100 and 140 MPa are 313 ± 288 and 65 ± 12. The observed increases in the exchange constant values with decreasing pressure are consistent with the enhanced mass transfer of

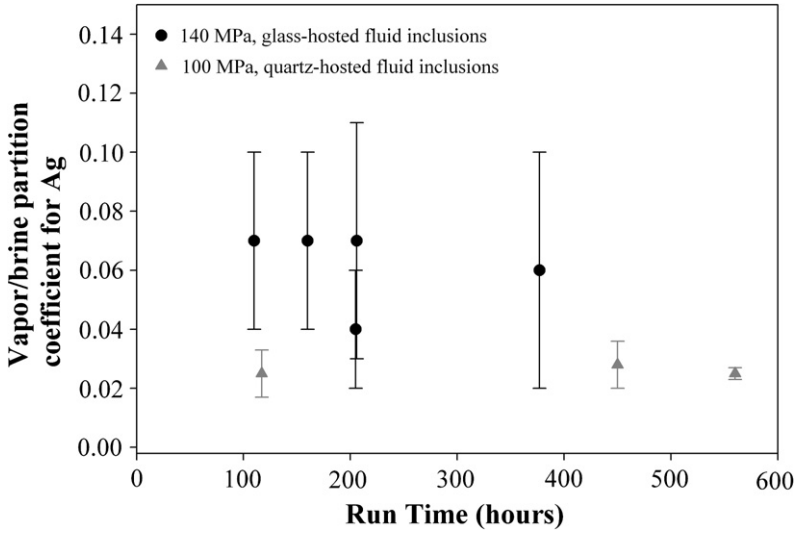

Fig. 5. The experimentally-determined partition coefficients for silver between coexisting vapor and brine as a function of run duration at 800 °C and $f_{O_2} \approx$ NNO. Uncertainties represent twice the standard error of the mean.

Table 6
Calculated values ($\pm 2\sigma$) for the apparent exchange constant describing silver–sodium exchange between the aqueous fluid and the silicate melt

Run No.	P (MPa)	$K^{v/m}_{Ag,Na}$	$K^{b/m}_{Ag,Na}$
4	140	17 (7.5)	74 (28)
5	140	14 (6.4)	62 (15)
6	140	16 (4.3)	67 (24)
7	130	9 (4.3)	59 (17)
14	140	14 (8.6)	61 (25)
Mean		14 (6)	65 (12)
19	100	84 (37)	234 (152)
22	100	59 (24)	NC
23	100	132 (59)	472 (280)
24	100	141 (98)	NC
25	100	108 (58)	225 (103)
Mean		105 (68)	313 (288)

NC, not calculated; brine inclusions were not analyzed in these glass run products.

silver from the silicate melt to the aqueous phases, both vapor and brine, during decompression. The calculated K value for run 7 does not follow this trend. Run 7 was held at 140 MPa for 157 h, but it slowly depressurized to 130 MPa over the final 48 h of the run lost pressure at the end of the experiment; the total run time was 205 h. The concentration of silver in run 7 vapor and sodium in the glass are lower than all other runs at 140 MPa and this may be attributed to the pressure drop and result in the decrease in the calculated $K^{v/m}_{Ag,Na}$ value. The general trend of increasing values of $K^{v/m}_{Ag,Na}$ with decreasing pressure has been observed in other experimental studies of copper, iron and gold and rare earth elements (Urabe, 1985; Webster et al., 1989; Williams et al., 1995; Simon et al., 2005). The enhanced partitioning of silver from rhyolite melt to both vapor and brine at 100 MPa, in agreement with the extant experimentally-determined partitioning behavior of gold and copper, suggests that the ore potential of an evolving silicate melt is maximized at depths on the order of 4 km which corresponds to the depth range over which many porphyry–gold, –silver, and –copper deposits form (Hedenquist and Lowenstern, 1994; Seedorff et al., 2005). It should be noted that data from many natural porphyry–ore systems suggests that ore–metal-carrying aqueous fluids do evolve from magma at depths greater than 4 km (Seedorff et al., 2005), potentially up to 10 km (e.g., Butte; Rusk et al., 2004). Further, as discussed below, it is emphasized that the depth at which metal-carrying aqueous fluids evolve from a causative magma does not correspond to the depth at which ore deposition occurs. In many porphyry deposits (Ballantyne et al., 1997; Singer et al., 2005) the ratio of silver-to-gold exceeds unity and the data presented here, in combination with gold solubility data from Simon et al. (2005), demonstrate that the high silver to gold ratios may be a function of the higher solubility of silver relative to gold in both vapor and brine.

The mass transfer of silver from the silicate melt to vapor and brine, in the S-free system studied here, may be controlled by an equilibrium such as

$$AgO^{m}_{0.5} + HCl^{mvp} = AgCl^{mvp} + 0.5H_2O^{mvp} \quad (5)$$

where m and mvp stand for melt and magmatic volatile phase, respectively. The hypothesized presence of silver as the neutral AgCl species in the volatile phase and the positive correlation between HCl and silver is based on previous experimental studies which have demonstrated such a trend for metals such as Cu (Candela and Holland, 1984; Williams et al., 1995), Au (Frank et al., 2002 Simon et al., 2006, 2007b) and Fe (Simon et al., 2004, 2005). Apparent equilibrium constants for Eq. (5) were calculated and are presented in Table 7. The average vapor–melt values for $K^{v/m}_{Ag}(\pm 2\sigma)$ at 100 MPa and 140 MPa are 24 ± 38.5 and 2.2 ± 1.5, respectively. The average brine–melt values for $K^{b/m}_{Ag}(\pm 2\sigma)$ at 100 MPa and 140 MPa are 81 ± 101 and 29.5 ± 28, respectively. The

Table 7
Calculated values (± log 2σ) for the apparent equilibrium constant describing silver partitioning between aqueous vapor and/or brine and melt

Run No.	P (MPa)	Matrix	$K_{Ag}^{v/m}(\pm 2\sigma)$	$K_{Ag}^{b/m}(\pm 2\sigma)$
4	140	Glass	2.2 (0.4)	19.5 (0.4)
5	140	Glass	1.9 (0.2)	15.0 (0.3)
6	140	Glass	1.9 (0.2)	20.6 (0.8)
7	140	Glass	1.9 (0.7)	45.6 (2.7)
8	140	Glass	1.5 (0.3)	27.2 (1.2)
14	140	Glass	3.7(1.3)	48.8 (3.3)
Mean			2.2 (1.5)	29.5 (28)
19	100	Quartz	18.4 (3.3)	50.7 (1.0)
19		Glass	15.8 (2.8)	NC
22	100	Quartz	22.8 (4.1)	NC
22		Glass	11.3 (2.0)	NC
23	100	Quartz	69.5 (20.7)	139.4 (16.3)
23		Glass	28.4 (8.5)	NC
24	100	Glass	8.2 (0.3)	NC
25	100	Quartz	22.4 (4.5)	52.5 (2.3)
Mean			24 (38.5)	81 (101)

NC, not calculated; brine inclusions were not analyzed in these glass run products.

increase in equilibrium constant values for both vapor and brine agrees with our earlier conclusion that the mass transfer of silver from silicate melt to exsolved volatile phases is enhanced during decompression from 140 to 100 MPa. The observed behavior may be attributed to an increase in the a_{HCl}^{vapor} with decreasing pressure as observed in natural systems by Giggenbach (1975) among others and experimentally by Shinohara and Fujimoto (1994) and Williams et al. (1997) among others. Williams et al. (1997) found that the ratios of HCl/NaCl and HCl/KCl are higher in low-salinity vapor relative to brine implying preferential partitioning of HCl into vapor. We suggest that the silver-carrying capacity of vapor may increase with increasing peraluminosity of the melt, hence increasing HCl content of the vapor. Future experiments at lower ASI values are planned to test this hypothesis.

4.2. The effect of pressure on the partitioning of silver between vapor and brine

The partitioning of silver between vapor and brine is evaluated here by comparing calculated partition coefficients, $D_{Ag}^{v/b}$, which are presented in Table 8 and shown in Fig. 5. The average calculated partition coefficients, $D_{Ag}^{v/b}(\pm 2\sigma)$, at 100 and 140 MPa are 0.026 ± 0.004 and 0.06 ± 0.03, respectively. The increase in $D_{Ag}^{v/b}$ with increasing pressure agrees with the constraint that the value of $D_{Ag}^{v/b}$ must trend toward and become unity at the critical pressure, ~160 MPa at 800 °C. The data demonstrate that pressure, hence total salinity, of the volatile phase, plays a determinant role in the partitioning of silver between vapor and brine in agreement with predictions based on the experimentally constrained partitioning of other ore metals (Candela and Holland, 1984; Frank et al., 2002; Simon et al., 2005, 2006). This finding has important implications for ore deposit genesis.

Table 8
Calculated Nernst-type partition coefficients ($\pm 2\sigma$) for silver between coexisting vapor, brine and melt

Run No.	P (MPa)	Matrix	$D_{Ag}^{v/m}(\pm 2\sigma)$	$D_{Ag}^{b/m}(\pm 2\sigma)$	$D_{Ag}^{v/b}(\pm 2\sigma)$
4	140	Glass	33 (16)	452 (240)	0.07 (0.04)
5	140	Glass	26 (10)	374 (77)	0.07 (0.03)
6	140	Glass	25 (16)	393 (67)	0.06 (0.04)
7	140	Glass	22 (10)	505 (156)	0.04 (0.02)
14	140	Glass	30 (16)	471(166)	0.07 (0.03)
Mean[a]			23 (10)	413 (172)	0.06 (0.03)
19	100	Quartz	31 (10)	1288 (531)	0.025 (0.008)
19		Glass	31 (10)	NC	NC
22	100	Quartz	20 (8)	NC	NC
22		Glass	11 (6)	NC	NC
23	100	Quartz	61 (19)	2140 (676)	0.028 (0.008)
23		Glass	21 (4)	NC	NC
24	100	Glass	35 (16)	NC	NC
25	100	Quartz	27 (8)	1095 (339)	0.025 (0.002)
25		Glass	49 (24)	NC	NC
Mean[a]		Glass	29 (28)[a]		
Mean[b]		Quartz	40 (36)[b]	1151 (238)[2]	0.026 (0.004)[2]

Run conditions as given in Table 1. NC, not calculated because brine inclusions, while present, were not analyzed in these glass run products (see text for discussion). The uncertainty in the mean reflects two times the deviation of the mean.

[a] This is the mean for glass-hosted fluid inclusions and melt for runs 19 through 25.

[b] This is the mean for quartz-hosted fluid inclusions and melt for runs 19 through 25.

The exsolution of either a low-density or high-density chlorine-bearing aqueous fluid from a silicate melt is controlled by the ratio of H_2O to Cl in the melt (cf. Candela and Piccoli, 1995; Webster, 2004). Silicate melts may saturate with and exsolve either a low-density Cl-bearing aqueous fluid, if the melt has a high initial H_2O/Cl ratio, or a high-density Cl-rich fluid (i.e., a brine or salt melt) if the melt has a low initial H_2O/Cl ratio. In the case where the melt has a high H_2O/Cl ratio, the melt will exsolve a low-density chlorine-bearing aqueous fluid. As this fluid evolves and ascends through the magma column and into the overlying country rock, the fluid may separate into immiscible vapor and brine if the single-phase aqueous fluid intersects the solvus during adiabatic decompression (cf. Bodnar et al., 1985; Candela and Piccoli, 1995). Following phase separation, silver will be partitioned between the low-density phase (i.e., vapor) and high-density phase (i.e., brine). If phase separation does not occur in the magma chamber, the low-density aqueous fluid (i.e., vapor) may achieve critical percolation and form an interconnected vapor plume which advects to the apical portions of the magma chamber (Candela, 1991). If this low-density aqueous fluid accumulates near the top of the magma chamber and significant overpressure of the gas phase occurs (Burnham, 1967), the fluid may hydrofracture the earlier formed igneous

solidification front and overlying country rock and ascend along self-propagating fractures. During ascent, ore metal precipitaition will take place either in the solification front or in the country rock owing to decompression, loss of heat and/or water–rock reaction.

The evolution of a single-phase, low-density, aqueous fluid from a magma chamber has been documented in natural fluid inclusion assemblages at the Butte (Montana, U.S.A.; Rusk et al., 2004) and Bingham (Utah, U.S.A.; Redmond et al., 2004) porphyry-Cu deposits. In both of these ore systems, the authors conclude that the causative magma evolved a single-phase aqueous fluid which scavenged and transported metals from the melt upward in the overlying porphyry environment where deposition occurred owing to changes in *PTX*. The low-density fluids at Butte have salinities ranging from approximately 3 to 4 wt% NaCl and those at Bingham from approximately 2 to 7 wt% NaCl equiv The silver solubility data presented here suggest that magmatic, low-density, chlorine-bearing aqueous fluid may scavenge enough silver, and other metals, to form a silver-rich porphyry ore deposit over the time-integrated life of a large magmatic system (cf. Richards, 2005); see discussion below. The presence of sulfur in the magmatic aqueous fluid (cf. Heinrich et al., 1999; Simon et al., 2006) may act to amplify the silver-carrying capacity of the aqueous fluid.

4.3. Estimating the total mass of silver carried by the volatile phases

The data presented above allow us to calculate the total tonnage of silver which may be delivered by the vapor to the porphyry environment for the case wherein melt degasses low-density vapor at 100 MPa, the upper pressure limit for porphyry deposits. According to Candela and Piccoli (1995), a melt with a chlorine/water ratio equal to or greater than 0.05 will exsolve a brine. For melts with lower chlorine to water ratios, only a vapor or supercritical gas would be exsolved from the melt. The calculated tonnage of silver which may be scavenged and transported from the magma chamber to the porphyry regime is based on the equation

$$E(Ag) = \left[\frac{C^{l,0}_{H_2O}}{C^{l,s}_{H_2O}}\right]^{\overline{D}_{Ag}} \times \left[1 + \frac{\overline{D}_{Ag}}{C^{l,s}_{H_2O} \times D^{v/m}_{Ag}}\right]^{-1} \quad (6)$$

originally presented and discussed in Candela and Holland, 1986. Eq. (6) allows one to calculate the efficiency with which vapor and brine can scavenge silver from a silicate melt as a function of the bulk partition coefficient $\overline{D}_{Ag}$, the ratio of the initial water concentration ($C^{l,0}_{H_2O}$) to the saturation water concentration ($C^{l,s}_{H_2O}$), and the Nernst-type partition coefficient for silver between vapor and melt ($D^{v/m}_{Ag}$) and brine and melt ($D^{v/m}_{Ag}$). The equation assumes a constant partition coefficient value; if the partition coefficients varies as a function of the concentration of Cl, HCl, H_2S, *inter alia*, as is the likely the case for natural systems, then the accuracy of the calculation is reduced. Note that if some proportion of silver in the silver nuggets in the silicate glass represents a stable phase at run conditions, then the calculated partition coefficients used in the modeling underestimate the total quantity of silver which may be scavenged by the vapor or brine. The experiments described here did not address the role of sulfides; these experiments are in progress. The presence of reduced sulfur in the vapor phase may increase the mass transfer of silver from the melt to the vapor (Pearson, 1963; Heinrich et al., 1999; Simon et al., 2006). Therefore, to calculate properly the ability of the volatile phase(s) to scavenge and advect silver from the silicate melt, we used pyrrhotite/melt partition coefficients from Englander (2005), $D^{po/m}_{Ag} = 2000$ at 800 °C and saturated vapor pressure(svp). Using this value for $D^{po/m}_{Ag}$ and the value for $D^{mt/m}_{Ag} = 10^{-4}$ calculated from data reported here, the quantity of silver scavenged by vapor from a 10 km^3 melt, which contains 1 μg/g silver (Gao et al., 1998) and crystallizes at 100 MPa, is 2×10^{12} g silver if magnetite and pyrrhotite constitute 2 and 0.02 mass % of the fractionating assemblage. Increasing the mass abundances of both magnetite and pyrrhotite to 10 and 0.1 %, respectively, affects only minimally the silver-scavenging capacity of the vapor; 1×10^{12} g of silver is scavenged in this case.

A melt volume of 10 km^3 most likely underestimates significantly the total, time-integrated volume of melt involved in the formation of porphyry- and epithermal-ore deposits. Richards (2005) suggests that epithermal- and porphyry-type ore deposits result from the punctuated differentiation of melt volumes on the order of tens to hundreds of km^3. Thus, the metal content of bonanza-type ore deposits is not the product of degassing of a single, static magma chamber, but rather the time-integrated flux of a magmatic centre which may degas for 10^4–10^5 years (cf. Arribas et al., 1995; Simmons and Brown, 2006). Halter et al. (2002) estimate a melt volume on the order of 15 km^3 to supply the Cu budget at Bajo de la Alumbrera. Using their melt volume estimate, a low-density vapor phase may scavenge on the order of 7×10^{12} g of silver from the melt; this is far greater than the 2×10^9 g (Singer et al., 2005) of silver in the deposit. Data from other deposits yield similar results. For example, the La Escondida (Chile), Bingham Canyon (Utah) and Batu Hijau (Philippines) porphyry deposits contain on the order of 2×10^{10}, 1×10^{10} and 1×10^9 g of silver, respectively (Singer et al., 2005). These model calculations above suggest that the low-density vapor maintains high silver concentrations as it ascends through the porphyry environment. Thus, it is reasonable to explore the possibility that the quantity of silver remaining in the vapor after porphyry formation may be responsible for the development of structurally higher, silver-rich high-sulfidation epithermal ore deposits.

Some high-sulfidation epithermal deposits have recently been proposed to represent the lower temperature and pressure near-surface component of a porphyry-epithermal continuum (cf. Muntean and Einaudi, 2001; Heinrich et al., 2004; Williams-Jones and Heinrich, 2005). Possible type localities for this continuum are found in the Refugio District in the Maricunga Belt, Northern Chile (Muntean and Einaudi, 2001) and at the Lepanto epithermal–Far Southeast porphyry deposits in northern Luzon, Philippines (Mancano and Campbell, 1995; Hedenquist et al., 1998).

Evidence for a magmatic origin for the aqueous fluid responsible for mineralization at both deposits includes spatial association, fluid inclusion characteristics and overlapping mineralization ages and stable isotope systematics. Muntean and Einaudi (2001) propose a model wherein low-density, aqueous fluid evolves from the causative magma at a depth on the order of 6 km (lithostatic pressure of 150 MPa) and temperatures in excess of 800 °C; note that this *PT* regime is closely constrained by the experiments in the current study. This low-density, magmatic aqueous fluid ascends adiabatically and intersects the solvus at a depth on the order of 5 km where phase separation occurs at a temperature of approximately 700 °C yielding low(er) density aqueous vapor and high-density aqueous brine. As these fluids continues to ascend, the rupturing of the brittle-ductile boundary causes the vapor and brine to flash to vapor and salt driving the precipitation of gold at *PT* conditions appropriate for the formation of a porphyry ore deposit. Sulfur is partitioned dominantly into the low-density vapor phase during the flashing process minimizing the precipitation of sulfides from the aqueous fluids. The sulfur- and metal-rich low-density aqueous fluid continues to ascend across the brittle-ductile boundary where decompression and phase separation at hydrostatic pressure results in metal deposition at *PT* conditions appropriate for the formation of an epithermal ore deposit. Fluid inclusion data from Lepanto indicate that mineralization occurred as ascending low-density magmatic vapor (salinities on the order 2–4 wt% NaCl equiv and Th ranging from 295 to 166 °C), which has been proposed as the metal-carrying fluid responsible for the Far Southeast porphyry deposit at depth, mixed with overlying meteoric water which caused precipitation of silver (Mancano and Campbell, 1995; Hedenquist et al., 1998). Mancano and Campbell (1995) and Hedenquist et al. (1998) conclude that the low-density vapor alone, in the absence of brine, was responsible for mineralization at Lepanto. While the current hypotheses for the development of the Far Southeast and Lepanto systems remain controversial, owing to the need for low-density aqueous fluid to migrate laterally, the data in this study lend plausibility to the hypothesis that their metal endowments are consistent with the evolution of a single magmatic, low-density aqueous fluid.

The ability of low-density aqueous vapor to transport significant quantities of silver, as species such as $AgCl_2^-$ (Gammons and Williams-Jones, 1995a,b) or $AgCl(H_2O)_3^v$ (Migdisov et al., 1999) at epithermal conditions has been confirmed by several experimental studies (Seward, 1976; Zotov et al., 1987; Levin, 1991; Gammons and Williams-Jones, 1995a,b; Gammons and Yu, 1997; Migdisov et al., 1999). For example, Gammons and Williams-Jones, 1995a,b report concentrations of silver up to 4×10^4 μg/g in aqueous HCl–NaCl solutions at 300 °C and saturated vapor pressure. Model calculations using data from the current study suggest that low-density vapor may scavenge on the order of 7×10^{12} g of silver from 15 km^3 of melt. If the vapor loses on the order of one-half of this silver during cooling and decompression through the porphyry regime, there remains sufficient silver to satisfy the budget of typical silver-rich, high-sulfidation epithermal deposits. There are no published data constraining the total silver budget at Lepanto. Combined, the deposits at Lepanto and Far Southeast contain on the order of 685 Mt of ore grade rock. Assuming that the deposits contain equal quantities of ore, and using the grade of 11 g/tons silver for Lepanto reported in Hedenquist et al. (1998), we calculate that Lepanto may contain on the order of 8×10^9 g silver. Thus, the calcualted mass of low-density vapor which may evolve from 15 km^3 of silicate melt could contain approximately three orders of magnitude more silver, by mass, than that present discovered at the combined Lepanto-Far Southeast deposits. Larger silver -rich, high-sulfidation deposits such as the Au–Ag–Cu Pascua deposit, containing approximately 2×10^{16} g silver, in the El Indio belt of north-central Chile and Argentina require a greater melt volume. Chouinard et al. (2005) conclude, on the basis of detailed field relations, geochronology and fluid inclusion data, that silver mineralization at Pascua may be attributed solely to ascending magmatic vapor. The integrated lifetime of the hydrothermal system responsible for gold, copper and silver deposition at Pascua was on the order of 10^6 million years (Bissig et al., 2001; Deyell et al., 2005). Silver mineralization is dominated by chloride salts and associated intimately with mercury, an element which displays a strong affinity for the low-density volatile phase during degassing (Chouinard et al., 2005). A melt volume on the order of 100 km^3, consistent with Richards (2005), is required to satisfy the silver budget of Pascua. Based on the protracted lifetime of hydrothermal activity of Pascua, it is feasible that degassing from such an integrated melt volume is mechanistically plausible.

5. CONCLUSIONS

Pressure affects strongly the partitioning of silver in a melt–vapor–brine assemblage. At 800 °C, $f_{O_2} \approx$ NNO the solubility of silver in rhyolite decreases as pressure decreases from 140 to 100 MPa. Nernst-type partition coefficient values calculated from the new experimental data suggest that the mass transfer of silver from rhyolite to exsolved vapor and brine is enhanced with a pressure drop from 140 to 100 MPa at magmatic temperatures. These data suggest that the potential for an evolving magmatic system to generate silver-rich porphyry and epithermal deposits is maximized when aqueous fluid saturation of the "parent" melt occurs at lower pressures; i.e., 100 MPa relative to 150 MPa. Model calculations suggest that low-density aqueous vapor alone, in the absence of magmatic brine, may transport a sufficient quantity of silver to satisfy the silver budget of many world-class porphyry and epithermal deposits. If low-density aqueous vapor ascends from a shallow-level magma (i.e., the causative intrusion) and undergoes phase separation owing to decompression, then this may be a highly efficient mechanism to continually supply silver, and other metals, to the porphyry and epithermal environments. We do not minimize the potentially important role that brine may play in transporting metals from a causative pluton to the porphyry and epithermal environment. Rather, we highlight that the new data for the silver-carrying capacity of low-density aqueous fluid, when

coupled with field (Redmond et al., 2004) and modeling (Heinrich et al., 2004) studies suggest a potentially significant role for low-density aqueous fluids in the development of silver-rich porphyry- and epithermal-ore deposits.

ACKNOWLEDGMENTS

This work was partially supported by National Science Foundation Grants: EAR 0609550 to A.C.S.; EAR 0440226 to P.A.C. and P.M.P.; and EPMA by EAR 9810244 to P.M.P. and others. The Fluid and Ore Deposits Group at ETH acknowledges continued support for LA-ICPMS analytical development by the Swiss National Science Foundation. We especially thank Jim Webster, John Dilles, Pedro Jugo and one anonymous scientist for their insightful and very helpful reviews.

REFERENCES

Acosta-Vigil A., London D., Morgan G. B. and Dewers, VI, T. A. (2003) Solubility of excess alumina in hydrous granitic melts in equilibrium with peraluminous minerals at 700–800 °C and 200 MPa, and applications of the aluminum saturation index. *Contrib. Mineral. Petrol.* **146**, 100–119.

Akinfiev N. N. and Zotov A. V. (2001) Thermodynamic description of chloride, hydrosulfide, and hydroxo complexes of Ag(I), Cu(I), Au(I) at temperatures of 25–600 °C and pressures of 1–2000 bar. *Geochem. Int.* **39**, 990–1006.

Anderko A. and Pitzer K. S. (1993) Equation-of-state representation of phase equilibria and volumetric properties of the system NaCl–H_2O above 573 K. *Geochim. Cosmochim. Acta* **57**, 1657–1680.

Archibald S. M., Migdisov A. A. and Williams-Jones A. E. (2002a) The stability of Au-chloride complexes in water vapor at elevated temperatures and pressures. *Geochim. Cosmochim. Acta* **65**(23), 4413–4423.

Archibald S. M., Migdisov A. A. and Williams-Jones A. E. (2002b) An experimental study of the stability of copper chloride complexes in water vapor at elevated temperatures and pressures. *Geochim. Cosmochim. Acta* **66**(9), 1611–1619.

Arribas, Jr., A., Hedenquist J. W., Itaya T., Okada T., Concepción R. A. and Garcia, Jr., J. S. (1995) Contemporaneous formation of adjacent porphyry and epithermal Cu–Au deposits over 300 ka in northern Luzon, Philippines. *Geology* **23**(4), 337–340.

Audétat A., Günther D. and Heinrich C. A. (1998) Formation of a magmatic hydrothermal ore deposit; insights in with LA–ICP–MS analysis of fluid inclusions. *Science* **279**, 2091–2094.

Audétat A., Günther D. and Heinrich C. A. (2000) Magmatic-hydrothermal evolution in a fractionating granite: a microchemical study of the Sn–W–F-mineralized Mole Granite (Australia). *Geochim. Cosmochim. Acta* **64**, 3373–3393.

Audétat A. and Pettke T. (2003) The magmatic–hydrothermal evolution of two barren granites: a melt and fluid inclusion study of the Rito del Medio and Cañada Pinabete plutons in northern New Mexico (USA). *Geochim. Cosmochim. Acta* **67**, 97–121.

Bailey D. K., Cooper J. P. and Knight J. L. (1974) Anhydrous melting and crystallization of peralkaline obsidians. *Bull. Volcanol.* **38**, 653–665.

Bailey D. K. and Cooper J. P. (1978) Comparison of the crystallization of pantelleritic obsidian under hydrous and anhydrous conditions. In: *Progress in Experimental Petrology: Fourth Progress Report of Research Supported by N.E.R.C., 1975–1978* (ed. W. S. MacKenzie), pp. 230–233.

Baker L. and Rutherford M. J. (1996) Crystallisation of anhydrite-bearing magmas. *Proc. Roy. Soc. Edinburgh: Earth Sci.* **87**, 243–250.

Ballantyne G. H., Smith T. W. and Redmond P. E. (1997) Gold and silver in the Bingham Canyon porphyry copper deposit, Utah. *Geol. Soc. Am. Abstr. Prog.* **29**, 283.

Belonoshko A. B., Shi P. F. and Saxena S. K. (1992) A FORTRAN-77 program for calculation of Gibbs free energy and volume of C–H–O–S–N–Ar mixtures. *Comp. Geosci.* **18**, 1267–1269.

Bissig T., Lee J. K. W., Clark A. H. and Heather K. B. (2001) The Cenozoic history of volcanism and hydrothermal alteration in the Central Andean flat-slab region: new 4° Ar-39Ar constraints from the El-Indio-Pascua Au (−Ag, Cu) belt, 29°20′–30°30′ S. *Int. Geol. Rev.* **43**, 312–340.

Bodnar R. J. and Sterner S. M. (1985) Synthetic fluid inclusions in natural quartz. II. Application to PVT studies. *Geochim. Cosmochim. Acta* **49**, 1855–1859.

Bodnar R. J. and Sterner S. M. (1987) Synthetic fluid inclusions. In *Hydrothermal Experimental Techniques* (eds. G. C. Ulmer and H. L. Barnes). John Wiley and Sons, New York, pp. 423–457.

Bodnar R. J., Burnham C. W. and Sterner S. M. (1985) Synthetic fluid inclusions in natural quartz. III. Determination of phase equilibrium properties in the system H_2O–NaCl to 1000 C and 1500 bars. *Geochim. Cosmochim. Acta* **49**, 1861–1873.

Bodnar R. J. and Vityk M. O. (1994) Interpretation of microthermometric data for H_2O–NaCl fluid inclusions. In *Fluid Inclusions in Minerals, Methods and Applications* (eds. B. De Vivo and M. L. Frezzotti), pp. 117–130. Fluid Inclusions in Minerals, Methods and Applications. Virginia Polytechnic Institute, VA.

Borisov A. and Palme H. (1997) Experimental determination of the solubility of platinum in silicate melts. *Geochim. Cosmochim. Acta* **61**(20), 4349–4357.

Burnham C. W. (1967) Hydrothermal fluids at the magmatic stage. In *Geochemistry of hydrothermal ore deposits* (ed. H. L. Barnes). Holt, Rinehart, Winston, NewYork, p. 670.

Burnham C. W. (1979) Magmas and hydrothermal fluids. In *Geochemistry of Hydrothermal Ore Deposits* (ed. H. L. Barnes). Wiley, New York, pp. 71–136.

Camprubi A., Chomiak B. A., Villanueva-Estrada R. E., Canals A., Norman D. I., Cardellach E. and Stute M. (2006a) Fluid sources for the La Buitarra epithermal deposit (Temascaltepec district, Mexico): volatile and helium isotope analyses in fluid inclusions. *Chem. Geol.* **3**, 252–284.

Camprubi A., González-Partida, Iriondo A. and Levresse G. (2006b) Mineralogy, fluid characteristics, and deposition environment of the Paleocene epithermal Au–Ag deposits of the El Barqueño District, Jalisco, Mexico. *Econ. Geol.* **101**, 235–247.

Candela P. A. (1990) Theoretical constraints on the chemistry of the magmatic aqueous phase. *Geol. Soc. Am. Paper* **246**, 11–20.

Candela P. A. (1991) Physics of aqueous phase exsolution in plutonic environments. *Am Min.* **76**, 1081–1091.

Candela P. A. and Holland H. D. (1984) The partitioning of copper and molybdenum between melts and aqueous fluids. *Geochim. Cosmochim. Acta* **48**, 373–380.

Candela P. A. and Holland H. D. (1986) A mass transfer model for copper and molybdenum in magmatic-hydrothermal systems: the origin of porphyry-type ore deposits. *Econ. Geol.* **81**, 1–19.

Candela P. A. and Piccoli P. M. (1995) Model ore–metal partitioning from melts into vapor and vapor/brine mixtures. In: Magmas, Fluids, and Ore Deposits, vol. 23 (ed. J. F. H. Thompson). Mineralogical Association of Canada Short Course, pp. 101–128.

Candela P. A. and Piccoli P. M. (2005) Magmatic processes in the development of porphyry-type ore systems. In: (eds. J. W.

Hedenquist, J. F. H. Thompson, R. J. Goldfarb and J. P. Richards). Econ. Geol. 100th Anniv. Vol., pp. 25–38.

Carmichael I. S. E. and MacKenzie W. S. (1963) Feldspar–liquid equilibria in pantellerites: an experimental study. *Am. J. Sci.* **261**, 382–396.

Charles R. W. and Vidale R. (1982) Temperature calibration of a new rapid quench vessel. *Am. Miner.* **67**, 175–179.

Chou I. C. (1987a) Phase relations in the system NaCl–KCl–H_2O. III. Solubilities of halite in vapor-saturated liquids above 445 degrees C and redetermination of phase equilibrium properties in the system NaCl–H_2O to 1000 degrees C and 1500 bars. *Geochim. Cosmochim. Acta* **51**, 1965–1975.

Chou I. C. (1987b). Oxygen buffer hydrogen sensor techniques at elevated pressures and temperatures. In: *Hydrothermal Experimental Techniques* (eds. G. C. Ulmer and H. L. Barnes), pp. 61–99.

Chou I.-M., Sterner S. M. and Pitzer K. S. (1992) Phase relations in the system NaCl–KCl–H_2O. IV. Differential thermal analysis of the sylvite liquidus in the KCl–H_2O binary, the liquidus in the NaCl–KCl–H_2O ternary, and the solidus in the NaCl–KCl binary to 2 kb pressure, and a summary of experimental data for thermodynamic-*PTX* analysis of solid–liquid equilibria at elevated *P–T* conditions. *Geochim. Cosmochim. Acta* **56**, 2281–2293.

Chouinard A., Williams-Jones A. E., Leonardson R. W., Hodgson C. J., Silva P., Tellez C., Vega J. and Rojas F. (2005) Geology and genesis of the multistage high-sulfidation epithermal Pascua Au–Ag–Cu deposit, Chile and Argentina. *Econ Geol.* **100**(3), 463–490.

Clemente B., Scaillet B. and Pichavant M. (2004) The solubility of sulphur in hydrous rhyolitic melts. *J. Petrol.* **45**(11), 2171–2196.

Cottrell E. and Walker D. (2006) Constraints on core formation from Pt partitioning in mafic silicate liquids at high temperatures. *Geochim. Cosmochim. Acta* **70**, 1565–1580.

Deyell C. L., Leonardson R., Rye R. O., Thompson J. F. H., Bissig T. and Cooke D. R. (2005) Alunite in the Pascua-Lama high-sulfidation deposit: constraints on alteration and ore deposition using stable isotope geochemistry. *Econ Geol* **100**, 131–148.

Dilles J. H. (1987) Petrology of the Yerington Batholith, Nevada: evidence for evolution of porphyry copper ore fluids. *Econ. Geol.* **82**(7), 1750–1789.

Emmons W. H. (1927) Relations of disseminated copper ores in porphyry to igneous intrusions. *Am. Inst. Mining Metall. Eng. Trans.* **75**, 797–809.

Englander L. (2005) An experimental study of silver partitioning in sulfide–oxide–melt systems at 800 °, C.M.S. Thesis, University of Maryland.

Ertel W., O'Neill H. St. C., Sylvester P. J. and Dingwell D. B. (1999) Solubilities of Pt and Rh in a haplobasaltic silicate melt at 1300 °C. *Geochim. Cosmochim. Acta* **63**(16), 2439–2449.

Fortefant S. S., Gunther D., Dingwell D. B. and Rubie D. C. (2003) Temperature dependence of Pt and Rh solubilities in a haplobasaltic melt. *Geochim. Cosmochim. Acta* **67**(1), 123–131.

Frank M. R., Candela P. A., Piccoli P. M. and Glascock M. D. (2002) Gold solubility, speciation, and partitioning as a function of HCl in the brine–silicate melt–metallic gold system at 800 °C and 100 MPa. *Geochim. Cosmochim. Acta* **66**, 3719–3732.

Gaillard F., Scaillet B., Pichavant M. and Beny J. M. (2001) The effect of water and fO_2 on the ferric–ferrous ratio of silicic melts. *Chem. Geol.* **174**, 255–273.

Gammons C. H. and Barnes H. L. (1989) The solubility of Ag_2S in near-neutral aqueous sulfide solutions at 25 to 300 °C. *Geochim. Cosmochim. Acta* **53**, 279–290.

Gammons C. H. and Williams-Jones A. E. (1995a) Hydrothermal geochemistry of electrum: thermodynamic constraints. *Econ. Geol.* **90**, 420–432.

Gammons C. H. and Williams-Jones A. E. (1995b) The solubility of Au–Ag alloy + AgCl in HCl/NaCl solutions at 300 C: new data on the stability of Au(I) chloride complexes in hydrothermal solutions. *Geochim. Cosmochim. Acta* **59**, 3453–3468.

Gammons C. H. and Yu Y. (1997) The stability of silver bromide and iodide complexes at 25 °C to 300 °C: experiments, theory and geologic applications. *Chem. Geol.* **137**, 155–173.

Gammons C. H., Yu Y. and Williams-Jones A. E. (1997) The disproportionation of gold(I) chloride complexes at 25 to 200 C. *Geochim. Cosmochim. Acta* **61**(10), 1971–1983.

Giggenbach W. F. (1975) Variations in the carbon, sulfur and chlorine contents of volcanic gases from White Island. *N.Z. Bull. Volcanol.* **39**, 15–27.

Giggenbach W. F. (1992) Magma degassing and mineral deposition in hydrothermal systems along convergent plate boundaries. *Econ. Geol.* **87**, 1927–1944.

Günther D., Frischknecht R., Heinrich C. A. and Kahlert H. J. (1997) Capabilities of an Argon fluoride 193 nm excimer laser ablation inductively coupled plasma mass spectrometry microanalysis of geological materials. *J. Anal. Atom. Spectrom.* **12**, 939–944.

Günther D., Audétat A., Frischknecht A. and Heinrich C. A. (1998) Quantitative analysis of major, minor, and trace elements in fluid inclusions using laser ablation-inductively coupled plasma mass spectrometry. *J. Anal. Atom. Spectrom.* **13**, 263–270.

Halter W. E., Pettke T. and Heinrich C. A. (2002) The origin of Cu/Au ratios in porphyry-type ore deposits. *Science* **296**, 1842–1844.

Halter W. E., Heinrich C. A. and Pettke T. (2005) Magma evolution and the formation of porphyry Cu–Au ore fluids: evidence from silicate and sulfide melt inclusions. *Miner. Deposit.* **39**, 845–863.

Hedenquist J. W. and Lowenstern J. B. (1994) The role of magmas in the formation of hydrothermal ore deposits. *Nature* **370**, 519–527.

Hedenquist J. W., Arribas, Jr., A. and Reynolds T. J. (1998) Evolution of an intrusion centered hydrothermal system: far Southeast-Lepanto porphyry and epithermal Cu-Au deposits, Philippines. *Econ. Geol.* **93**, 373–404.

Heinrich C. A. (2007). *Fluid–fluid interactions in magmatic–hydrothermal ore formation* **65**(1), 363–387.

Heinrich C. A., Ryan C. G., Mernagh T. P. and Eadington P. J. (1992) Segregation of ore metals between magmatic brine and vapor. *Econ. Geol.* **87**, 1566–1583.

Heinrich C. A., Günther D., Audétat A., Ulrich T. and Frischknecht R. (1999) Metal fractionation between magmatic brine and vapor, determined by microanalysis of fluid inclusions. *Geology* **27**, 755–758.

Heinrich C. A., Pettke T., Halter W. E., Aigner-Torres M., Audétat A., Günther D., Hattendorf D., Bleiner D., Guillong M. and Horn I. (2003) Quantitative multi-element analysis of minerals, fluid and melt inclusions by laser-ablation inductively-coupled-plasma mass spectrometry. *Geochim. Cosmochim. Acta* **67**, 3473–3497.

Heinrich C. A., Driesner T., Stefansson A. and Seward T. M. (2004) Magmatic vapor contraction and the transport of gold from the porphyry environment to epithermal ore deposits. *Geology* **32**(9), 761–764.

Henley R. W. and McNabb A. (1978) Magmatic vapor plumes and ground-water interaction in porphyry copper emplacement. *Econ. Geol.* **73**, 1–20.

Holland H. D. (1972) Granites, solutions, and base metal deposits. *Econ. Geol.* **67**, 281–301.

Huebner J. S. and Sato M. S. (1970) The oxygen fugacity–temperature relationships of manganese oxide and nickel oxide buffers. *Amer. Miner.* **55**, 934–938.

Jarosewich E., Nelen J. A. and Norbery J. A. (1980) Reference samples for electron microprobe analsyes. *Geostand. Newslett.* **4**, 43–47.

Jugo P. J., Candela P. A. and Piccoli P. M. (1999) Magmatic sulfides and Au:Cu ratios in porphyry deposits: an experimental study of copper and gold partitioning at 850 °C, 100 MPa in a haplogranitic melt–pyrrhotite–intermediate solid solution–gold metal assemblage, at gas saturation. *Lithos* **46**, 573–589.

Kozlov V. K., Kuznetsov V. N. and Khodakovskiy I. K. (1983) The thermodynamic parameters of Ag_2O (c) and silver (I) hydroxy complexes in aqueous solution at elevated temperatures. *Geokhimiya* **2**, 215–227.

Kruger Y. and Diamond L. W. (2001) Unexpected behavior of fluid inclusions synthesized from silver oxalate and an aqueous NaCl solution. *Geochim Cosmochim. Acta* **173**(1–3), 159–177.

Liebscher A. and Heinrich C. A. (2007). *Fluid–fluid interactions in the Earth's lithosphere* **65**(1), 1–13.

Levin K. A. (1991) An experimental and thermodynamic study of the stabilities of silver chloride complexes in KCl and NaCl solutions up to 7 m at 300 C. *Geokhimiya* **10**, 1463–1468.

Levin K. A. (1994) Thermodynamic properties of silver chloride complexes. *Geochem. Int.* **13**, 41–47.

Longerich H. P., Jackson S. E. and Gunther D. (1996) Laser ablation inductively coupled plasma mass spectrometric transient signal data acquisition and analyte concentration calculation. *J. Anal. Atom. Spectrom.* **11**, 899–904.

Lynton S. J., Candela P. A. and Piccoli P. M. (1993) An experimental study of the partitioning of copper between pyrrhotite and a high silica rhyolitic melt. *Econ. Geol* **88**, 901–915.

Mancano D. and Campbell A. R. (1995) Microthermometry of enargite hosted Fluid Inclusions from the Lepanto Philippines high sulfidation Cu–Au deposit. *Geochim. Cosmochim. Acta* **59**, 3909–3916.

Margolis J. and Britten R. M. (1995) Porphyry-style and epithermal copper–molybdenum–gold–silver mineralization in the northern and southeastern Sulphurets district, northwestern British Columbia. In: *Porphyry Deposits of the Northwestern Cordillera of North America*, vol. 46 (ed. T. G. Schroeter). Canadian Institute of Mining, Metallurgy and Petroleum Special Volume, pp. 499–508.

Marschik R. and Fontboté L. (2001) The candelaria-punta del cobre iron oxide Cu–Au (–Zn–Ag) deposits. Chile. *Econ. Geol.* **96**, 1799–1826.

McMillan P. F. and Holloway J. R. (1987) Water solubility in aluminosilicate melts. *Contrib. Miner. Petrol.* **97**, 320–332.

Migdisov A. A., Williams-Jones AE. and Suleimenov O. M. (1999) Solubility of chlorargyrite (AgCl) in water vapor at elevated temperatures and pressures. *Geochim. Cosmochim. Acta* **63**, 3817–3827.

Morgan, VI, G. B. and London D. (1996) Optimizing the electron microprobe analysis of hydrous alkali aluminosilicate glasses. *Amer. Miner.* **81**, 1176–1185.

Muntean J. L. and Einaudi M. T. (2001) Porphyry–epithermal transition: Maricunga belt, northern Chile. *Econ. Geol.* **96**, 743–772.

Mysen B. O. (1991) Volatiles in magmatic liquids. In *Progress in Metamorphic and Igneous Petrology* (ed. L. L. Perchuk). Cambridge University Press, Cambridge.

Nokleberg W. J., Bundtzen T. K., Brew D. A. and Plafker G. (1995) Metallogenesis and tectonics of porphyry copper, molybdenum (gold, silver), and granitoid-hosted gold deposits of Alaska. In: *Porphyry Deposits of the Northwestern Cordillera of North America*, vol. 46 (ed. T. G. Schroeter). Canadian Institute of Mining, Metallurgy and Petroleum Special Volume, pp. 103–141.

Okamato H. (1997) Ag–Pt (Silver–Platinum). *J. Phase Equilib.* **18**, 485.

Orville K. L. and Shelton P. M. (1980) Formation of synthetic fluid inclusions in natural quartz. *Amer. Miner.* **65**(11–12), 1233–1236.

Pearce N. J. G., Perkins W. T., Westgate J. A., Gorton M. P., Jackson S. E., Neal C. R. and Chenery S. P. (1997) A compilation of new and published major and trace element data for NIST SRM 610 and NIST SRM 612 glass reference materials. *Geostandard. Newslett.* **21**, 115–144.

Pearson R. G. (1963) Hard and soft acids and bases. *J. Am. Chem. Soc.* **85**, 3533–3543.

Pettke T., Heinrich C. A., Ciocan A. C. and Gunther D. (2000) Quadrupole mass spectrometry and optical emission spectroscopy: detection capabilities and representative sampling of short transient signals from laser-ablation. *J. Anal. Atom. Spectrom.* **15**(9), 1149–1155.

Pettke T., Halter W. E., Driesner T., von Quadt A. and Heinrich C. A. (2001) The porphyry to epithermal link: preliminary fluid chemical results from the Apuseni Mountains, Romania, and Famatina, Argentinian Andes. In: *Eleventh Annual V.M. Goldschmidt Conference*.

Pettke T., Halter W. E., Webster J. D., Aigner-Torres M. and Heinrich C. A. (2004) Accurate quantification of melt inclusion chemistry by LA-ICPMS: a comparison with EMP and SIMS and advantages and possible limitations of these methods. *Lithos* **78**, 333–361.

Rainbow A., Clark A. H., Kyser T. K., Gaboury F. and Hodgson C. J. (2005) The Pierina epithermal Au–Ag deposit, Ancash, Peru: paragenetic relationships, alunite textures, and stable-isotope geochemistry. *Chem. Geol.* **215**(1–4), 235–252.

Redmond P. B., Einaudi M. T., Inan E. E., Landtwing M. R. and Heinrich C. A. (2004) Copper deposition by fluid cooling in intrusion-centered systems: new insights from the Bingham porphyry ore deposit, Utah. *Geology* **32**(3), 217–220.

Requia K., Stein H., Fontboté L. and Chiaradia M. (2003) Re–Os and Pb–Pb geochronology of the Archean Salobo iron oxide–copper–gold deposit, Carajás mineral province, northern Brazil. *Miner. Deposit.* **38**, 727–738.

Richards J. P. (2005) Cumulative factors in the generation of giant calc-alkaline porphyry Cu deposits. In *Super Porphyry Copper and Gold Deposits—A Global Perspective*, vol. 1 (ed. T. M. Porter). PGC Publishing, Adelaide, pp. 7–25.

Richards J. P., McCulloch M. T., Chappell B. W. and Kerrich R. (1991) Sources of metals in the Porgera gold deposit, Papua New Guinea; evidence from alteration, isotope, and noble metal geochemistry. *Geochim. Cosmochim. Acta* **55**, 580–656.

Repel K. U., Migdisov A. A. and Williams-Jones A. E. (2006) The solubility and speciation of molybdenum in water vapor at elevated temperatures and pressures: implications for ore genesis. *Geochim. Cosmochim. Acta* **70**, 687–696.

Roedder E. (1984) Fluid Inclusions. *Rev. Mineral.* **12**, 644.

Rusk B. G., Reed M. H., Dilles J. H., Klemm L. M. and Heinrich C. A. (2004) Compositions of magmatic hydrothermal fluids determined by LA-ICP-MS of fluid inclusions from the porphyry copper–molybdenum deposit at Butte, MT. *Chem. Geol.* **210**(1–4), 173–199.

Scaillet B. and MacDonald R. (2001) Phase relations of peralkaline silicic magmas and petrogenetic implications. *J. Petrol.* **42**, 825–845.

Seedorff E., Dilles J. D., Proffett, Jr., J. M., Einaudi M. T., Zürcher L., Stavast W. J. A., Johnson D. A. and Barton M. D. (2005) Porphyry deposits: characteristics and origin of hypogene features. *Econ. Geol.* **100**, 251–298.

Seward T. M. (1976) The stability of chloride complexes of silver in hydrothermal solutions up to 350 °C. *Geochim. Cosmochim. Acta* **40**, 1329–1341.

Shinohara H. and Fujimoto K. (1994) Experimental study in the system albite–andalusite–quartz NaCl–HCl–H_2O at 600 °C and 400–2000 bars. *Geochim. Cosmochim. Acta* **58**, 4857–4866.

Shinohara H. and Hedenquist J. W. (1997) Constraints on magma degassing beneath the Far Southeast porphyry Cu–Au deposit, Philippines. *J. Petrol.* **38**, 1741–1752.

Shinohara H. and Kazahaya K., (1995) Degassing processes related to magma-chamber crystallization. In: *Magmas, Fluids and Ore Deposits*, vol. 23 (ed. J. F. H. Thompson). Mineralogical Association of Canada Short Course, pp. 47–70.

Sillitoe R. H. (1979) Some thoughts on gold-rich porphyry copper deposits. *Miner. Deposit.* **14**, 161–174.

Sillitoe R. H. (1989) Gold deposits in western Pacific island arcs; the magmatic connection. *Econ. Geol. Monogr.* **6**, 274–291.

Sillitoe R. H. (1993a) Epithermal models: genetic types, geometric controls and shallow features. In: *Mineral Deposit Modeling Kirkham*, vol. 40 (eds. R. V. Kirkham, W. D. Sinclair, R. I. Thorpe and J. M. Duke). Geological Association of Canada Special Volume, pp. 403–417.

Sillitoe, R.H., 1993b. Gold-rich porphyry copper deposits: geological model and exploration implications. In: *Mineral Deposit Modeling*, vol. 40 (eds. R. V. Kirkham, W. D. Sinclair, R. I. Thorpe and J. M. Duke). Geological Association of Canada Special Volume, pp. 465–478.

Sillitoe R. H. (2000) Gold-rich porphyry deposits: descriptive and genetic models and their role in exploration and discovery. *Rev. Econ. Geol.* **13**, 315–345.

Simmons S. F. and Brown K. L. (2006) Gold in magmatic hydrothermal solutions and the rapid formation of a giant ore deposit. *Science* **314**, 288–291.

Simmons S. F., White, N. C. and John D. A. (2005) Geological characteristics of epithermal. In: *Econ. Geol.* (eds. Hedenquist J. W., Thompson J. F. H., Goldfarb R. J. and Richards J. P.), 100th Anniv. vol. pp. 485–522.

Simon A. C., Frank M. R., Pettke T., Candela P. A., Piccoli P. M., Heinrich C. A. and Glascock M. (2007a) An evaluation of synthetic fluid inclusions for the purpose of trapping equilibrated, coexisting, immiscible fluid phases at magmatic conditions. *Amer. Miner.* **92**, 124–138.

Simon A. C., Pettke T., Candela P. A., Piccoli P. M. and Heinrich C. (2007b) The partitioning behavior of As and Au in a haplogranite–vapor at magmatic conditions in sulfur-free and sulfur bearing systems. *Geochim. Cosmochim. Acta* **71**, 1764–1782.

Simon A. C., Pettke T., Candela P. A., Piccoli P. M. and Heinrich C. (2006) Copper partitioning in sulfur bearing magmatic systems. *Geochim. Cosmochim. Acta* **70**, 5583–5600.

Simon A. C., Pettke T., Candela P. A., Piccoli P. M. and Heinrich C. A. (2005) Gold partitioning in melt–vapor–brine systems. *Geochim. Cosmochim. Acta* **69**, 3321–3335.

Simon A. C., Pettke T., Candela P. A., Piccoli P. M. and Heinrich C. A. (2004) Magnetite solubility and iron transport in magmatic–hydrothermal environments. *Geochim. Cosmochim. Acta* **68**, 4905–4914.

Simon A. C., Pettke T., Candela P. A., Piccoli P. M. and Heinrich C. A. (2003) Gold solubility in magnetite: preliminary implications for magmatic gold budgets. *Am. Miner.* **88**, 1644–1651.

Singer D. A. (1995) World class base and precious metal deposits: a quantitative analysis. *Econ. Geol.* **90**, 88–104.

Singer D. A., Cox D. P., (1986) Grade and tonnage model of porphyry copper–gold deposits. In: *Mineral Deposit Models*, vol. 1693 (eds. D. P. Cox and D. A. Singer). U.S. Geological Survey Bulletin, pp. 110–114.

Singer D. A., Berger V. I. and B. C. Moring (2005) USGS Open-File Report 2005–1060, Porphyry copper deposits of the world: Database, map and grade and tonnage models. <http://pubs.usgs.gov/of/2005/1060/>.

Sirbescu M-L. C. and Nabelek P. I. (2003) Crystallization conditions and evolution of magmatic fluids in the Harney Peak Granite and associated pegmatites, Black Hills, South Dakota—evidence from fluid inclusions. *Geochim. Cosmochim. Acta* **67**, 2443–2465.

Sourirajan S. and Kennedy G. C. (1962) The system NaCl–H_2O at elevated temperatures and pressures. *Am. J. Sci.* **260**, 115–141.

Spilsbury T. W. (1995) The Schaft creek copper–molybdenum–gold–silver porphyry deposit, northwestern British Columbia. In: *Porphyry Deposits of the Northwestern Cordillera of North America*, vol. 46. Canadian Institute of Mining, Metallurgy and Petroleum Special Volume, pp. 239–246.

Stefánsson A. and Seward T. M. (2003) Experimental determination of the stability and stoichiometry of sulphide complexes of silver(I) in hydrothermal solutions to 400 C. *Geochim. Cosmochim. Acta* **67**, 1395–1413.

Sterner S. M. and Bodnar R. J. (1984) Synthetic fluid inclusions in natural quartz. I: Compositional types synthesized and applications to experimental geochemistry. *Geochim. Cosmochim. Acta* **48**, 2659–2668.

Sterner S. M., Hall D. L. and Bodnar R. J. (1988) Synthetic fluid inclusions. V. Solubility relations in the system NaCl–KCl–H_2O under vapor-saturated conditions. *Geochim. Cosmochim. Acta* **52**, 989–1005.

Sterner S. M., Chou I.-M., Downs R. T. and Pitzer K. S. (1992) Phase relations in the system NaCl–KCl–H_2O. V. Thermodynamic–*PTX* analysis of solid–liquid equilibria at high temperatures and pressures. *Geochim. Cosmochim. Acta* **56**, 2295–2309.

Thompson R. N. and MacKenzie W. S. (1967) Feldspar–liquid equilibria in peralkaline acid liquids: an experimental study. *Am. J. Sci.* **265**, 714–734.

Thompson J. F. H., Lang J. R., Mortensen J. K. and Cassidy K. F. (1995) Cu–Au metallogeny of alkalic arc magmatism: examples from the Mesozoic arc terranes of the northern Canadian Cordillera and comparison to the Tabar-Feni arc, PNG. In: *Giant Ore Deposits-II Symposium*, Queen's University, Kingston, Ontario, April, 1995, pp. 668–673.

Titley S. R. (1981) Geological and geotectonic setting of porphyry copper deposits in the southern Cordillera. *Arizona Geol. Soc.* **14**, 79–97.

Ulrich T., Günther D. and Heinrich C. A. (2001) Evolution of a porphyry Cu–Au deposit, based on LA-ICP-MS analysis of fluid inclusions, Bajo de la Alumbrera, Argentina. *Econ. Geol.* **97**, 1888–1920.

Urabe T. (1985) Aluminous granite as a source of hydrothermal ore deposits: an experimental study. *Econ. Geol.* **80**, 148–157.

Vanko D. A., Bodnar R. J. and Sterner S. M. (1988) Synthetic fluid inclusions. VIII. Vapor-saturated halite solubility in part of the system NaCl–$CaCl_2$–H_2O, with application to fluid inclusions from oceanic hydrothermal systems. *Geochim. Cosmochim. Acta* **52**, 2451–2456.

Vennemann T. W., Muntean J. L., Kesler S. E., O'Neil J. R., Valley J. W. and Russell N. (1993) Stable isotope evidence for magmatic fluids in the Pueblo Viejo epithermal acid–sulfate Au–Ag deposit, Dominican Republic. *Econ. Geol.* **88**, 55–71.

Vila T. and Sillitoe R. H. (1991) Gold-rich porphyry systems in the Maricunga Belt, northern Chile. *Econ. Geol.* **86**, 1238–1260.

Watson E. B. (1994) Diffusion in volatile-bearing magmas. *Rev. Mineral.* **30**, 371–411.

Webster J. G. (1986) The solubility of gold and silver in the system Au–Ag–S–O_2–H_2O at 25 °C and 1 atm. *Geochim. Cosmochim. Acta* **50**, 1837–1845.

Webster J. D. (1992) Fluid–melt interactions involving Cl-rich granites: experimental study from 2 to 8 kbar. *Geochim. Cosmochim. Acta* **56**, 659–678.

Webster J. D. (2004) The exsolution of magmatic hydrosaline chloride liquids. *Chem. Geol.* **210**(1–4), 33–48.

Webster J. D., Holloway J. R. and Hervig R. L. (1989) Partitioning of lithophile trace elements between H_2O and H_2O–CO_2fluids and topaz rhyolite melt. *Econ. Geol.* **84**, 116–134.

Webster J. D. and Mandeville C. W. (2007) Fluid immiscibility in volcanic environments. *Rev. Min. Geochem.* **65**(1), 313–362.

Williams T. J., Candela P. A. and Piccoli P. M. (1995) The partitioning of copper between silicate melts and two-phase aqueous fluids: an experimental investigation at kbar, 800 °C and 0.5 kbar, 850 °C. *Contrib. Miner. Petrol.* **121**, 388–399.

Williams T. J., Candela P. A. and Piccoli P. M. (1997) Hydrogen-alkali exchange between silicate melts and two-phase aqueous mixtures: an experimental investigation. *Contrib. Miner. Petrol.* **128**, 114–126.

Williams-Jones A. E. and Heinrich C. A. (2005) Vapor transport and the formation of magmatic hydrothermal ore deposits. *Econ. Geol.* **100**, 1287–1312.

Zezin D. Y., Migdisov A. A. and Williams-Jones A. E. (2007) The solubility of gold in hydrogen sulfide gas: an experimental Study. *Geochim. Cosmochim. Acta* **71**(12), 3070–3081.

Wood S. A., Crerar D. A. and Borsik M. P. (1987) Solubility of the assemblage pyrite–pyrrhotite magnetite–sphalerite–galena–gold–stibnite–bismuthinite–argentite–molybdenite in H_2O–NaCl–CO_2 solutions from 200 C to 350 C. *Econ. Geol.* **82**, 1864–1887.

Zotov A. V., Levin K. A., Khodakovskiy I. L. and Kozlov Vl. K. (1987) Thermodynamic parameters of Ag(I) chloride complexes in aqueous solutions at 273–623 K. *Geochem. Int.* **24**, 103–116.

Associate editor: Edward M. Ripley